Cluster observations of fast shocks in the magnetosheath launched as a tangential discontinuity with a pressure increase crossed the bow shock

N C Maynard, C.J J Farrugia, D.M. Ober, W.J. Burke, M. Dunlop, F.S. Mozer, H. Reme, Pierrette Décréau, K.D. Siebert

Cluster observations of fast shocks in the magnetosheath launched as a tangential discontinuity with a pressure increase crossed the bow shock

N. C. Maynard,[1] C. J. Farrugia,[1] D. M. Ober,[2] W. J. Burke,[2] M. Dunlop,[3] F. S. Mozer,[4] H. Rème,[5] P. Décréau,[6] and K. D. Siebert[7]

Received 25 February 2008; revised 14 July 2008; accepted 24 July 2008; published 21 October 2008.

[1] The interaction of a tangential discontinuity (TD) and accompanying dynamic pressure increase with the Earth's bow shock launches a fast shock that travels ahead of the TD in the magnetosheath and carries a significant portion of the pressure change. In this event study, we use observations from the Cluster spacecraft and magnetohydrodynamic simulations to identify the fast shock and its properties and to track the TD in the magnetosheath. Velocities of the fast shock and the TD were determined by triangulation using the four distant Cluster spacecraft. The fast shock is a planar structure, traveling nearly perpendicular to **B** at the magnetosonic speed in the plasma rest frame. Changes in density and $|\mathbf{B}|$ are correlated, with about a 20% increase in each. A current was observed tangential to the plane of the fast shock, and the positive $\mathbf{E} \bullet \mathbf{J}$ there provided an electromagnetic energy source for the observed heating of the ions. The fast shock is generated by the pressure change and determines the timing of the initial response of the magnetopause to that change. The TD was moving nearly in the $-X_{\mathrm{GSE}}$ direction and was being compressed as it moved inward. The passage of the TD ushered in large-scale compressive structure in the magnetosheath magnetic field, which satisfied the mirror mode instability criterion. Velocities of a fast rarefaction wave, reflected from the magnetopause, and an additional slow-mode structure, which was not a product of the initial interaction with the bow shock, were determined by triangulation.

Citation: Maynard, N. C., C. J. Farrugia, D. M. Ober, W. J. Burke, M. Dunlop, F. S. Mozer, H. Rème, P. Décréau, and K. D. Siebert (2008), Cluster observations of fast shocks in the magnetosheath launched as a tangential discontinuity with a pressure increase crossed the bow shock, *J. Geophys. Res.*, *113*, A10212, doi:10.1029/2008JA013121.

1. Introduction

[2] On 29 April 2003, while the four Cluster spacecraft were in the dayside magnetosheath an interplanetary tangential discontinuity (TD) with a density increase impacted the bow shock. With each of the Cluster spacecraft separated by more than 4000 km, the event is ideal for investigating products of this interaction as they propagated through the magnetosheath. The theory of discontinuity interactions in collisionless plasmas is well established, but experimental verification near the bow shock and in the magnetosheath has been elusive. We use the multipoint capability of Cluster, when the interspacecraft separations are substantial, to provide a definitive confirmation.

[3] In the collisionless magnetosheath and solar wind, dynamic pressure perturbations are sources of magnetosonic waves. The speeds of these waves depend on their propagation directions with respect to the magnetic field [*Friedricks*, 1957; *Kantrovitch and Petschek*, 1966]. Slow-mode and Alfvén waves have zero phase velocity perpendicular to **B**. In the case studied here, where the Alfvén speed is larger than the sound speed, their maximum phase speeds occur along the field direction. The largest phase speeds of fast waves are achieved when their wave vectors **k** are perpendicular to **B**. Fast mode disturbances are initiated by local changes in the pressure and are characterized by in-phase changes of the wave's magnetic field and plasma density perturbations. They carry some of the pressure change across the background magnetic field. Conversely the magnetic field and density variations of slow-mode waves have opposite phases. They propagate at oblique angles to the background magnetic field and tend to reduce field-aligned pressure gradients [see *Kivelson and Russell*, 1995]. *Southwood and Kivelson* [1992, 1995] showed that a slow-mode structure may stand in the flow in the magnetosheath.

[1]Space Science Center, University of New Hampshire, Durham, New Hampshire, USA.
[2]Air Force Research Laboratory, Hanscom Air Force Base, Massachusetts, USA.
[3]Rutherford Appleton Laboratory, Didcot, UK.
[4]Space Science Laboratory, University of California, Berkeley, California, USA.
[5]CESR, CNRS, Toulouse, France.
[6]Laboratoire de Physique et Chimie de l'Environnement, Orleans, France.
[7]SPARTA Inc., Nashua, New Hampshire, USA.

0148-0227/08/2008JA013121

Table 1. Results of Minimum Variance Tests and the Ratios of B_n and $|\Delta B|$ to $|B|$, Following the Tests Described by *Neugebauer et al.* [1984] for Identifying the Character of Directional Discontinuities as Tangential, Rotational, or Either

Interval (UT)	Number	$B_n \pm \sigma$	λ	n Vector	$B_n/\|B\|$	$\|\Delta B\|/\|B\|$
			Wind			
1639–1641	40	−0.20 ± 0.44	3.3	0.80, 0.54, 0.26	0.02, 0.02	0.26, 0.36
1638–1642	80	−1.12 ± 0.40	2.6	0.66, 0.72, 0.21	0.10, 0.13	0.26, 0.36
1637–1643	120	−0.53 ± 0.39	3.2	0.74, 0.64, 0.23	0.05, 0.06	0.26, 0.36
			Cluster 1			
1736–1744		1.05 ± 1.78	5.7	0.989, −0.113, 0.092	0.01, 0.03	0.38, 0.63
			Cluster 4			
1738–1741	4036	0.81 ± 2.20	8.7	0.992, −0.081, 0.090	0.01, 0.02	0.38, 0.63
1738:36–1740:12	2170	0.61 ± 1.93	6.4	0.995, −0.026. 0.093	0.01, 0.02	0.38, 0.63

This is exemplified by a slow front that locally reduces the magnetic field upstream from the magnetopause. Near the subsolar magnetopause, $|\mathbf{B}|$ increases in depletion layers that form along stagnation streamlines [*Zwan and Wolf*, 1976].

[4] Large dynamic pressure changes are often associated with magnetic field discontinuities or shocks. Magnetic field directional discontinuities (DD) in the solar wind are classified as rotational (RD), tangential (TD), or either (ED) [e.g., *Neugebauer et al.*, 1984; *Neugebauer*, 2006]. Most EDs tend to resemble RDs. Tests for distinguishing TDs from RDs are given in each Table 1 of their articles. The most common test for a TD employs a minimum variance analysis [*Sonnerup and Cahill*, 1967] to show that the component of **B** normal to the discontinuity (B_n) is zero. On the other hand, an RD must have a significant B_n. A very small B_n is sometimes attributable to errors in the minimum variance analyses [*Lepping and Behannon*, 1980]. When this happens, other common tests based on the magnetic field are often used: for TDs (1) the ratio of $B_n/|\mathbf{B}|$ should be small (<0.2) and (2) the ratio of $\Delta B/|\mathbf{B}|$ large (>0.2), where ΔB is the change in magnitude of **B** across the discontinuity [*Neugebauer*, 2006]. The opposite relations apply for RDs. For EDs $B_n/|\mathbf{B}|$ and $\Delta B/|\mathbf{B}|$ are both small. Additional tests include the plasma quantities. The total pressure (plasma plus magnetic) should be the same on both sides of a TD. However, changes in plasma density and/or pressure anisotropy ($A = 1 - 4\pi\ (p_{\|} - p_{\perp})/\ |\mathbf{B}|^2$) are arbitrary for TDs. Across an RD the product of density and anisotropy must be constant. Besides identifying significant B_n through minimum variance, the most commonly used technique to establish that a DD is an RD is the Walén test [e.g., *Sonnerup et al.*, 1987]. A Walén test requires that changes from reference levels of the vector components $\Delta V_{i,j}$ and $\Delta A_{i,j}$ in the maximum and intermediate variance directions must be proportional with slopes of order ±1 (where $\Delta A_{i,j} = 21.806\ \Delta B\ (\mathrm{nT})/\mathrm{n}^{1/2}\ (/\mathrm{cc}^{1/2})$). The significance of a test is reduced to the degree that this ratio departs from ±1. The ratio is the inverse of the *Neugebauer* [2006] parameter R_{VB}, which is typically 0.4 to 0.6 or less for a TD and 0.6 to 0.8 for an ED. In the text below we use "DD" when referring to a discontinuity before positive classification or at magnetosheath locations where a TD may be transitioning to an RD [*Maynard et al.*, 2002, 2007; *Phan et al.*, 2007].

[5] When an interplanetary TD with an associated dynamic pressure change in the solar wind impacts the Earth's bow shock (itself a standing fast shock), the structure splits into two fast shocks that surround the discontinuity. The downstream fast shock travels ahead of the modified TD in the magnetosheath; the upstream shock is the bow shock itself migrating toward a new equilibrium position [*Völk and Auer*, 1974]. In this paper downstream (upstream) means a location toward the Earth (toward the Sun) from a feature. When the fast shock impacts the magnetopause it partially transmits into the lower-density magnetosphere and reflects as a fast rarefaction wave into the magnetosheath [e.g., *Grib et al.*, 1979; *Samsonov et al.*, 2007]. *Neubauer* [1975] studied the interaction of a TD with the bow shock with arbitrary normal orientation. Other products of the interaction, including slow waves, may be present when the interaction is between an RD and the bow shock [*Neubauer*, 1976]. Calculations by *Wu et al.* [1993] show that a TD with a twofold density increase produces a fast shock that carries density and magnetic field increases of about 18% above background, as well as a velocity increase of 35%. These percentages are variable, depending on the strength of the density increase. As a result of dynamic pressure changes, the magnetopause must find a new equilibrium position. The positional change starts when the fast shock reaches the magnetopause.

[6] *Maynard et al.* [2007] used magnetosheath measurements from the Polar spacecraft to characterize a fast wave generated during the interaction of a TD and associated density decrease with the bow shock. In that case the fast wave was a rarefaction wave surrounded by the two transition regions as predicted by *Völk and Auer* [1974]. In addition to correlated density and $|\mathbf{B}|$ decreases, *Maynard et al.* [2007] showed that ions were strongly accelerated along the magnetic field in the fast rarefaction wave and perpendicular to it in the transition layer on downstream side of the wave. They suggested that nonlinear effects were responsible for the strong accelerations. They also found that some part of the interplanetary TD structure evolved into a rotational discontinuity. Associated time-dependent magnetic merging within the magnetosheath was responsible for three bursts of field-aligned accelerated ions.

[7] This investigation focuses on a fast shock observed in the magnetosheath on 29 April 2003 and complements our previous study of a fast rarefaction wave. We present particle and magnetic and electric field data from the Cluster constellation and compare them with predictions of magnetohydrodynamic (MHD) simulations. Using the four spacecraft, we establish the velocity characteristics of the fast shock, the DD, and an additional wave structure encountered just downstream of it. We measure the fast shock

increase in density, $|\mathbf{B}|$, and velocity, demonstrate that it is planar in character, and show that it is a source of ion heating. However, this event did not manifest the strong ion acceleration found in the rarefaction wave case. Simulations show that the fast shock initiates an inward motion of the magnetopause toward the new equilibrium position required by increased pressure.

2. Measurement Techniques

[8] On 29 April 2003, at 1630 UT, the Wind spacecraft was located upstream in front of the Earth near the first Lagrangian point (L_1). Three-second resolution measurements were made of the ion density and ion velocity by the Three-Dimensional Plasma and Energetic Particle Investigation (3DPL) instrument [*Lin et al.*, 1995], and of the interplanetary magnetic field (IMF) by the fluxgate magnetometer of the Magnetic Field Investigation (MFI) [*Lepping et al.*, 1995]. Proton temperature anisotropies are from the Solar Wind Experiment (SWE) [*Ogilvie et al.*, 1995].

[9] Magnetic field measurements were made in the magnetosheath by triaxial fluxgate magnetometers on the four Cluster spacecraft [*Balogh et al.*, 2001]. The electric field and wave instrument (EFW) monitored both electric field components in the ecliptic plane using biased double probes [*Gustafsson et al.*, 1997]. The third component was calculated using the $\mathbf{E} \bullet \mathbf{B} = 0$ approximation (this assumes that the parallel electric field is very small, which is valid in most situations). The Cluster Ion Spectrometer (CIS) experiment provided 3-D ion distributions with mass per unit charge composition using the Composition and Distribution Function (CODIF) analyzer or 3-D ion distributions using the Hot Ion Analyzer [*Rème et al.*, 2001]. Ion measurements are available only from Cluster 1, 3, and 4. During the period of interest, the highest-resolution measurements were made by Cluster 4. High-resolution electron density measurements were made by the Whisper instrument using plasma wave techniques [*Décréau et al.*, 2001]. We also use the Cluster "Curlometer" analysis tool for determining the current by calculating curl **B** from the magnetometer measurements on all four spacecraft [*Dunlop et al.*, 2002].

3. Simulation Techniques

[10] The Integrated Space-Weather Model (ISM) uses standard MHD equations augmented with hydrodynamic equations for a collisionally coupled neutral thermosphere [*White et al.*, 2001]. The code transitions seamlessly from pure MHD for plasma in the solar wind and magnetosphere to proper ionosphere/thermosphere equations at low altitudes. ISM equations are solved within a three-dimensional computational domain extending from an interior spherical boundary at the approximate bottom of the E-layer (100 km) extending up through the magnetosphere and out into the solar wind. The spatial resolution of ISM's computational grid varies from a few hundred kilometers in the ionosphere to several R_E in the distant magnetotail downstream of the Earth. In the dayside magnetosphere and forward to the sunward boundary (40 R_E) the grid resolution was nearly uniform at 0.1 R_E resolution along the Earth-Sun line direction, which was necessary to resolve the discontinuity in the solar wind and resulting products of its interaction with the bow shock.

[11] Explicit viscosity was set equal to zero in the plasma momentum equation. An explicit resistivity term was included in Ohm's law only when the current density normal to **B** exceeded a specified threshold. In practice, this choice led to an explicit, nonzero resistivity only near the subsolar magnetopause, and in the nightside plasma sheet. Where dissipation is needed to maintain numerical stability, it arises via the partial donor-cell method (PDM) as formulated by *Hain* [1987]. Dissipation is also necessary in the code to approximate nonlinear magnetic merging. It is important to note that the code solves for the configuration imposed by the boundary conditions by adding dissipation. In simulations described here dissipation on the dayside was accomplished through PDM in response to the imposed driving conditions rather than a current-dependent resistivity term. A fuller description of the ISM code is found in *White et al.* [2001].

4. Observations

4.1. Interplanetary Data

[12] On 29 April 2003, the Wind satellite sampled a fast-streaming solar wind near L_1 with an above-average magnetic field strength. At the center of our interval of interest Wind was at (253, 38, 19) R_E (GSE coordinates). IMF and solar wind plasma data from 1630 to 1700 UT are presented in Figure 1. From top to bottom, the panels show the solar wind's density, bulk speed, temperature and dynamic pressure as well as the magnitude and three components of **B** in GSE coordinates. A discontinuity in the interplanetary magnetic field (IMF) accompanied by a sharp increase in density passed Wind at ~1640 UT. It was marked by a change in **B** in which its magnitude (Figure 1e) decreased from 11.4 to 8.4 nT, with a minimum of 6 nT near the center of the discontinuity. Components changed from (5.8, −3.3, −9.2) nT at 1639:15 UT to (0.1, −3.9, 7.4) nT at 1640:45 UT. We note that the change in B_Z occurred in two steps with a short interval of constant magnitude near the zero crossing (Figure 1h). While the magnetic field was changing direction and magnitude, the density (Figure 1a) increased from 2.8 to 7.0 cm^{-3}, as the dynamic pressure (Figure 1d) shifted from 1.4 to 3.7 nP. The ion velocity rose from 535 to 565 km/s with a peak at 580 km/s at the center of the discontinuity (Figure 1b). All quantities started to return toward their original values about 10 min later.

[13] We performed several of the tests described by *Neugebauer et al.* [1984] and *Neugebauer* [2006] to determine the nature of the DD. The total pressure (the sum of the magnetic, proton and electron pressures assuming quasi-neutrality and no alpha particles) is overlaid on Figure 1d in red. It is constant, within the accuracy of the measurements, as expected for a TD. A minimum variance analysis was performed on the 3-s resolution IMF data in the interval 1639 to 1641 UT [*Sonnerup and Cahill*, 1967]. A robust normal (**n**) was found with a ratio (λ) of intermediate-to-minimum eigenvalues of 3.3. The GSE components of **n** were (0.80, 0.54, 0.26). B_n was -0.20 ± 0.44 nT, consistent with zero. Two other nested analyses were performed with **n** within 17° of the original. For these two tests B_n was larger and above the 1-σ significance level. Because of a possibly

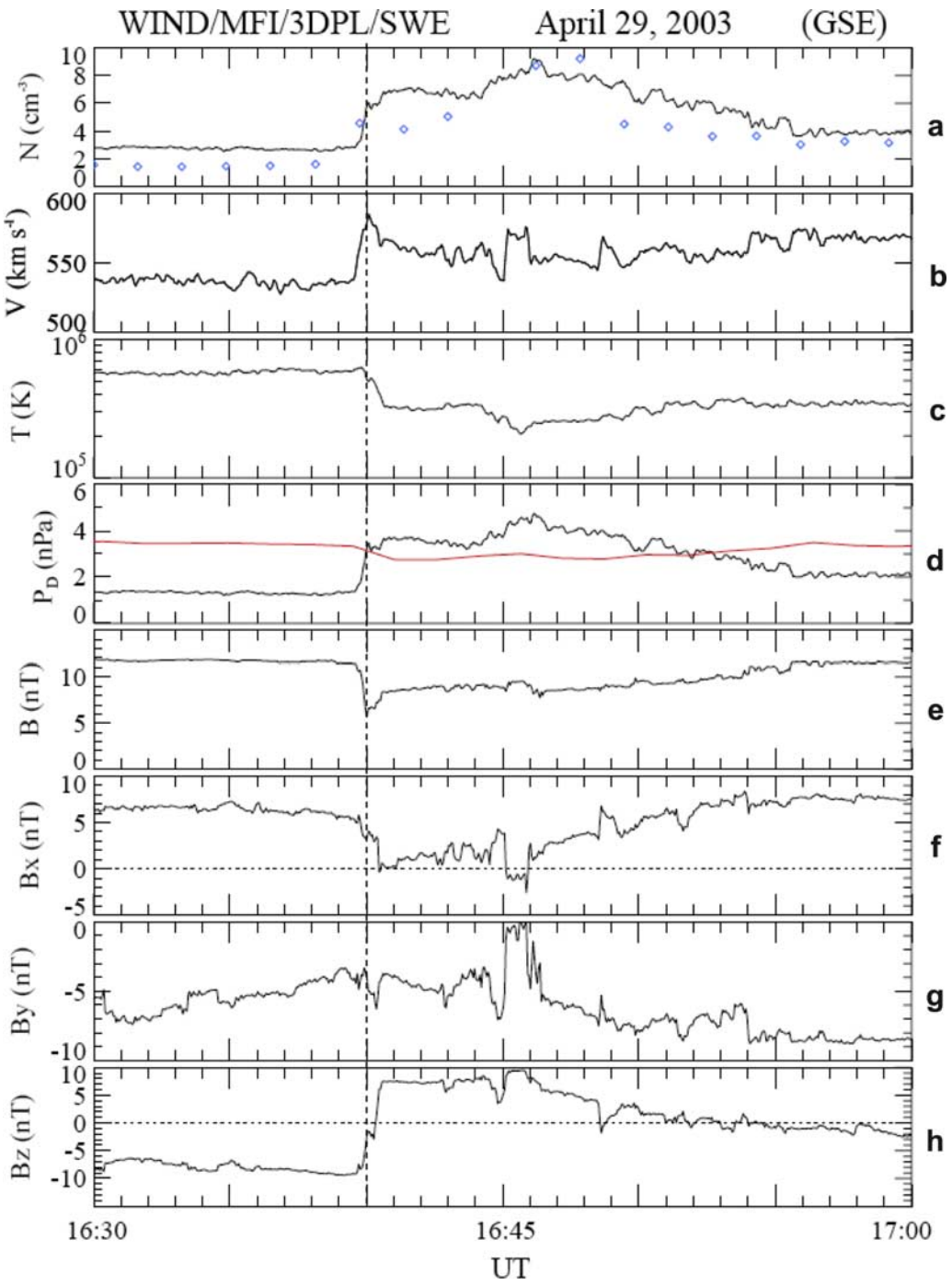

Figure 1. Solar wind and interplanetary magnetic field (IMF) data from the Wind satellite from 1615 to 1715 UT on 29 April 2003. (a–d) The solar wind density, proton velocity, proton temperature, and dynamic pressure from the 3-D plasma and energetic particle investigation. (e–h) The magnitude and three components of the magnetic field in GSE coordinates from the magnetic field instrument. Wind was located upstream near the L_1 point at coordinates of (253, 38, 19) R_E (GSE). Propagation time of the tangential discontinuity (TD) from Wind to Cluster was approximately 59 min. The blue dots in Figure 1a are the product of the density and the anisotropy ($A = 1 - 4\pi(p_{\|} - p_{\perp})/|\mathbf{B}|^2$). The red trace in Figure 1d is the sum of the magnetic and perpendicular plasma pressure, multiplied by a factor of 50.

significant B_n we performed Walén tests on both sides of the zero crossing of B_Z. The sign of the slope reversed as expected if the satellite were crossing the separatrices of an RD. However, we regard the test as inconclusive because the number of available data points was small, and the slopes were well away from unity, as well as being different between the i and j components. $B_n/|\mathbf{B}|$ was small and $\Delta\mathbf{B}/|\mathbf{B}|$ was large, consistent with a TD. Furthermore, the

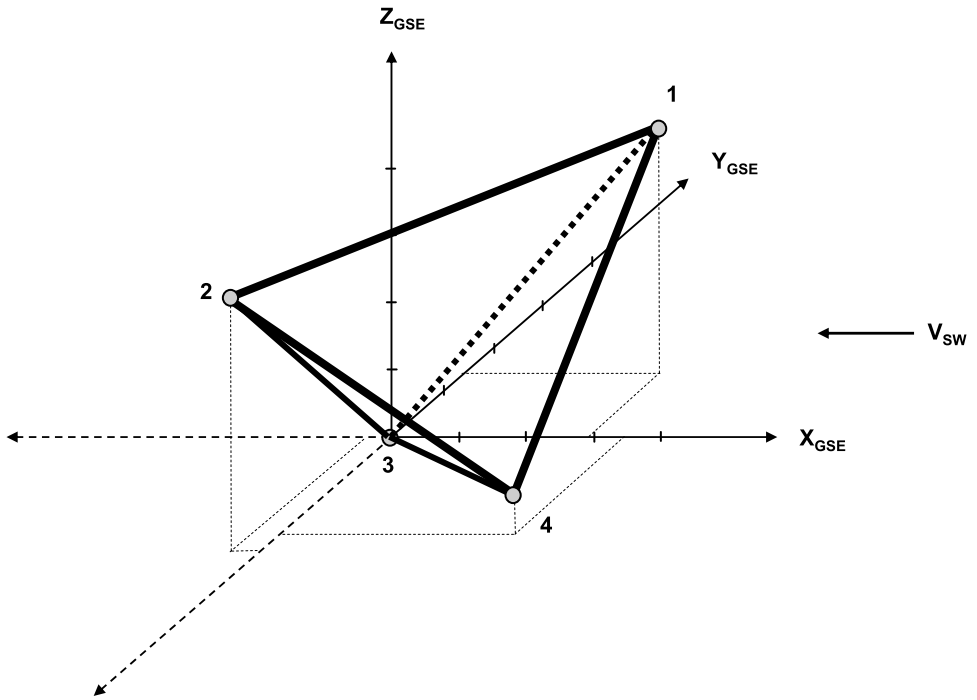

Figure 2. Schematic orientation of the four Cluster spacecraft relative to a coordinate system centered on Cluster 3 with axes parallel to the GSE axes. The tick marks on the axes are every 1000 km. Features flowing away from the bow shock in the magnetosheath will be seen first by Clusters 1 or 4 and then later by Clusters 2 and 3.

change in the product of the anisotropy and the density across the DD (blue dots in Figure 1a) was large. In aggregate the tests support our contention that the DD was a TD as it passed Wind. The results of these tests, as well as other minimum variance analyses discussed below, are given in Table 1. The ratios $B_n/|\mathbf{B}|$ and $\Delta\mathbf{B}/|\mathbf{B}|$ are shown in the Table 1 for values of $|\mathbf{B}|$ on both sides of the TD. The quantity λ should be greater than 2 for the errors in the minimum variance solution to be acceptable [*Lepping and Behannon*, 1980].

4.2. Cluster Observations

[14] At 1737 UT the Cluster constellation was in the magnetosheath north of the equatorial plane and on the dawn side of noon. The GSE coordinates of the reference satellite Cluster 3 were (7.6, −6.8, 6.4) R_E with separation distances from spacecraft 1, 2, and 4 of 4832, 4635, and 4047 km, respectively. Figure 2 shows the tetrahedral configuration of the four spacecraft. Cluster 4 was in the lead, followed closely by Clusters 1, and 3. Cluster 2 was last to encounter the structure. Interspacecraft separations >4000 km are sufficient to distinguish the details of a structure's motional characteristics.

[15] Figure 3 presents Cluster 1 observations of proton and electron densities, proton velocities and temperatures, as well as the magnitudes and three components of **B** in GSE coordinates. The discontinuity was observed at Cluster ~59 min after it passed Wind as indicated by an abrupt change in $|\mathbf{B}|$ and density at 1739 UT. The electron-density scale (Figure 3b) was expanded to emphasize details in the low-density region before the DD's arrival near 1739 UT, highlighted by the solid line. A minimum variance analysis, performed over the interval from 1736 to 1744 UT yielded a very reliable normal with a ratio (λ) of the intermediate-to-minimum eigenvalues of 5.7. The normal component of **B** was 1.047 ± 1.779 nT in a GSE direction (−0.989, 0.113, −0.0917), indicating that the structure had maintained the properties of a tangential discontinuity as it passed Cluster 1. We also checked the total pressure (proton and magnetic pressure using Cluster 4 data which had the highest-resolu-

Figure 3. Data from the Cluster 1 satellite from 1734 to 1744 UT, which spans the interval of the fast shock and TD (solid vertical line). (a) The ion density from CIS-HIA shows the large change at the TD, while (b) the electron density from Whisper is plotted on an expanded scale to emphasize variations associated with the fast shock (dashed line 2), a reflected fast rarefaction wave (dashed line 3), and a slow-mode structure (dashed lines 4 and 5). Dashed line 1 represents the start of an upward trend in density. The sum of the perpendicular plasma pressure and the magnetic pressure (red trace) multiplied by a factor of 50 is overlaid on Figure 3a with the pressure scale to the right. (d, f) The proton velocity and temperature. (g–j) The magnitude and three GSE components of the magnetic field. See text for explanation of the Q intervals. (c, e) The density and velocity measured by Wind with their timescales expanded by a factor of 2.42. This time expansion would be appropriate if the density increases at lines 1 and 2 both initiated fast shocks (see section 5.3).

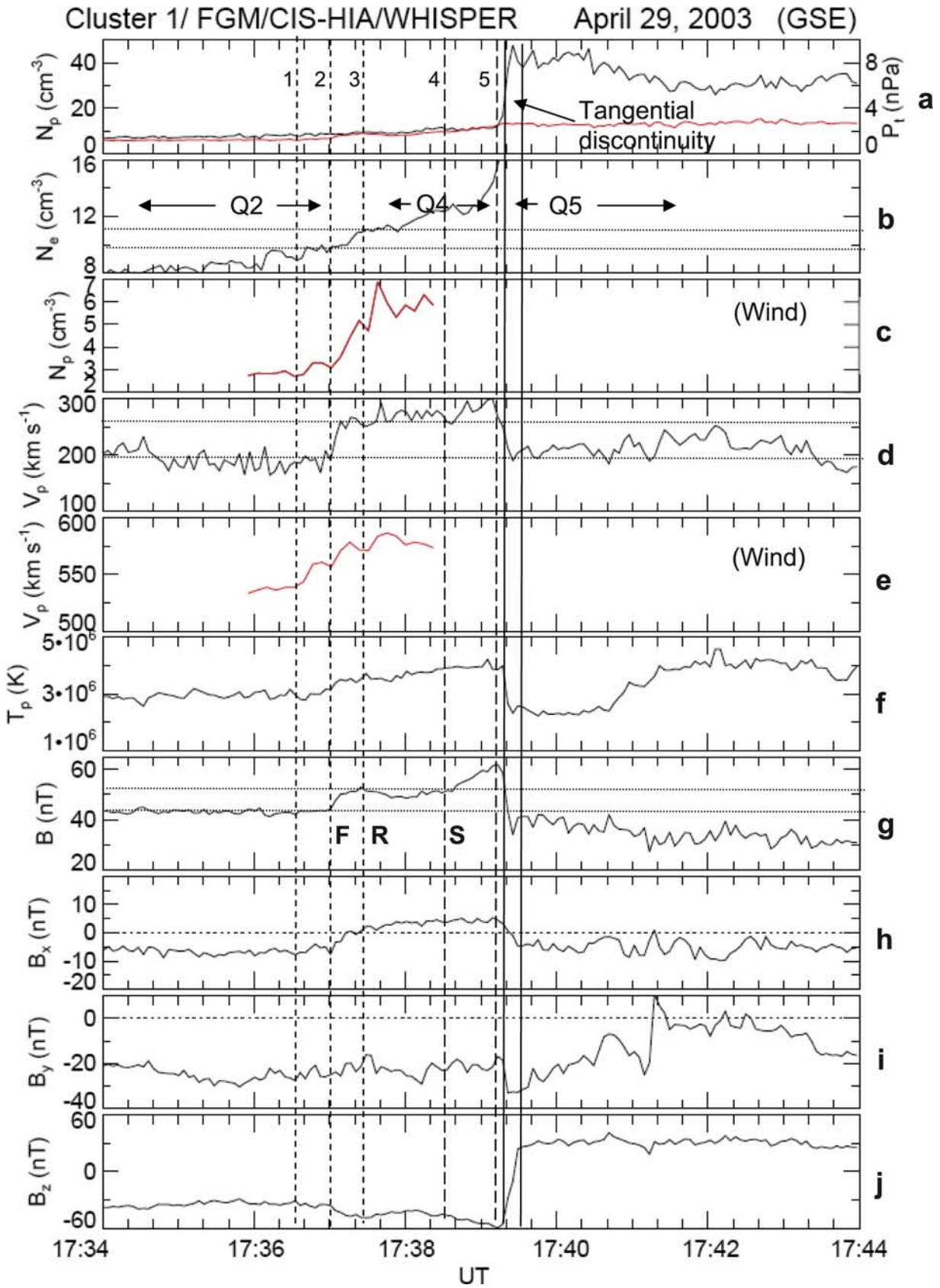
Cluster 1/ FGM/CIS-HIA/WHISPER April 29, 2003 (GSE)
1
2
3
4
5
Tangential discontinuity
Q2
Q4
Q5
(Wind)
F
R
S
UT
17:34
17:36
17:38
17:40
17:42
17:44

Figure 3

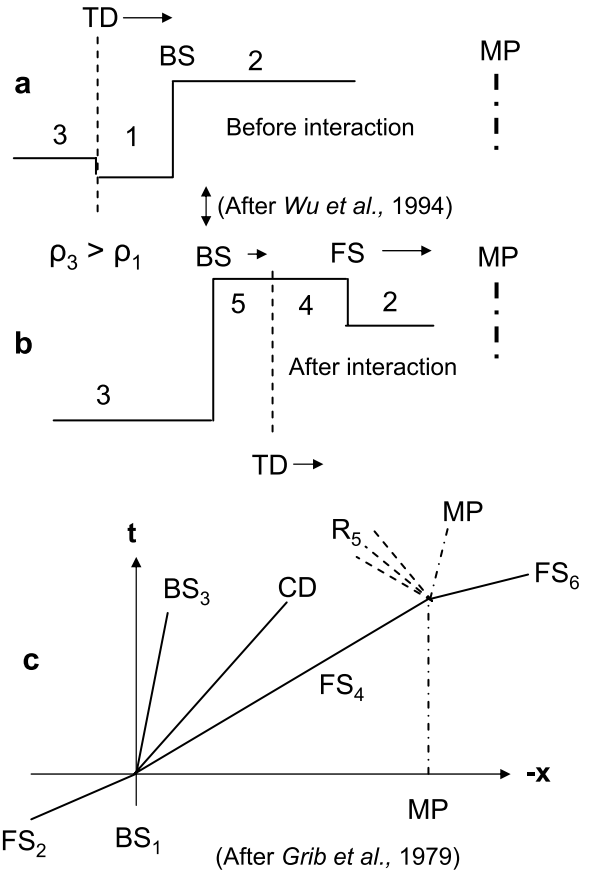

Figure 4. Schematic of a 1-D interaction of a TD with the bow shock described (a) just before the interaction takes place and (b) after the interaction following the notation of *Wu et al.* [1993]. Regions 1 and 2 encompass the preexisting solar wind and magnetosheath, respectively. Region 3 is upstream of the TD in the solar wind. Region 4 is between the fast wave and the transmitted TD, while Region 5 is between the modified bow shock and the transmitted TD in the magnetosheath. (c) The timeline for the interaction of a fast shock with the bow shock, including the subsequent interaction with the magnetopause, follows *Grib et al.* [1979, Figure 6]. The products of the interaction at the bow shock are the transmitted fast shock, a contact discontinuity, and the modified bow shock. With a magnetic field change, or TD, with the fast shock, the CD would be the transmitted TD. At the magnetopause, the products are a reflected fast rarefaction wave, a modified magnetopause, and a transmitted fast wave into the magnetosphere.

tion ion data) and found it to be constant within the accuracy of the measurements. A plot of the sum of the perpendicular plasma pressure and the magnetic pressure is overlaid (in red) in Figure 3a. $B_n/|\mathbf{B}|$ was also small (0.02) and $|\Delta\mathbf{B}|/|\mathbf{B}|$ was large (0.5), again indicating that the DD remained a TD until after it passed the Cluster spacecraft. Since the normal direction had a small southward component, the discontinuity must have first impacted the bow shock north of the ecliptic plane.

[16] *Völk and Auer* [1974] and *Wu et al.* [1993] predicted that the bow shock's interaction with a TD and accompanying density increase generates a fast shock that propagates ahead of the discontinuity in the magnetosheath. Between 1736:32 UT (vertical dashed line 1) and the arrival of the TD near 1739 UT Cluster detected an upward trend in the density. Attention is drawn to the sharper increases in $|\mathbf{B}|$, $|\mathbf{V}|$, and density (Figures 3g, 3d, and 3b) beginning near 1737 UT (highlighted by dashed line 2) and labeled F. Correlated variations of density and $|\mathbf{B}|$ are a characteristic of magnetosonic fast shocks, and we refer to this as a fast-shock (F) interval in the remainder of the paper as we explore its properties and justify this designation. After dashed line 3, $|\mathbf{B}|$ decreased slightly, but the density remained constant (thus, decreasing relative to the upward trend). Subsequently, the density and $|\mathbf{B}|$ resumed their increases.

[17] The fast shock carries a fraction of the density and $|\mathbf{B}|$ changes. The Q labels follow nomenclature introduced by *Wu et al.* [1993], where the Q denotes a parameter while the number refers to a region/interval. Figure 4 schematically shows the principal features (Figure 4a) before and (Figure 4b) after the interaction of the TD with the bow shock and labels with numbers the intervals upstream and downstream of the features. $Q2$ is representative of the interval/region downstream of the bow shock before the fast shock arrival. $Q4$ represents the interval/region between the fast shock and the TD. $Q5$ is the period/region sampled after the passage of the TD, and thus characterizes the properties of the magnetosheath plasma between Cluster and the bow shock. By taking the ratios of quantities sampled in intervals $Q4$ and $Q2$ [cf. *Wu et al.*, 1993, Table 1] we determine percentage increases. The cited model predicts increases in density, $|\mathbf{B}|$, and $|\mathbf{V}|$ carried by the fast shock of 18%, 18%, and 35%, respectively for a solar wind density jump of 2, which is somewhat smaller than the jump of 2.5 in the present event. Using the values highlighted by the horizontal dotted lines in Figures 3b, 3g, and 3d, Cluster measured increases of 18%, 20%, and 36% in these quantities. The total density jump from $Q2$ to $Q5$ was by a factor > 4.5; the total change in $|\mathbf{B}|$ was ~1. The TD in the solar wind carried a decrease in $|\mathbf{B}|$ of 25%.

[18] To investigate these features further, Figure 5 shows profiles of magnetic field magnitudes at the four Cluster spacecraft between 1735 and 1743 UT. The increase at the fast shock and the decrease at the TD are evident in the four traces, but occur at different times at each spacecraft. Beginning times for these features are marked by dashed line 2 and the solid line, respectively. (The dashed line numbering in this and subsequent figures is the same as that used in Figure 3). For all four traces dashed line 1 has been placed at the same time interval before line 2 as used in Figure 3. Note that it begins a gentle increase in $|\mathbf{B}|$ at each spacecraft as highlighted by the orange overlay (same slope and duration in each trace). This will be addressed further in the Discussion. At Cluster 4 the decrease at the TD (Figure 5d) started at ~1739:20 UT then recovered before making a sharp descent. Similar pauses appear in the data streams of the other three spacecraft at different positions on the TD descent. Because these pauses are at different positions and not at the zero crossing, we believe that this feature represents a separate wave structure and is unrelated to the step in the IMF B_Z observed at Wind. This wave structure on the TD complicates start time selections, but has no further significance in this paper.

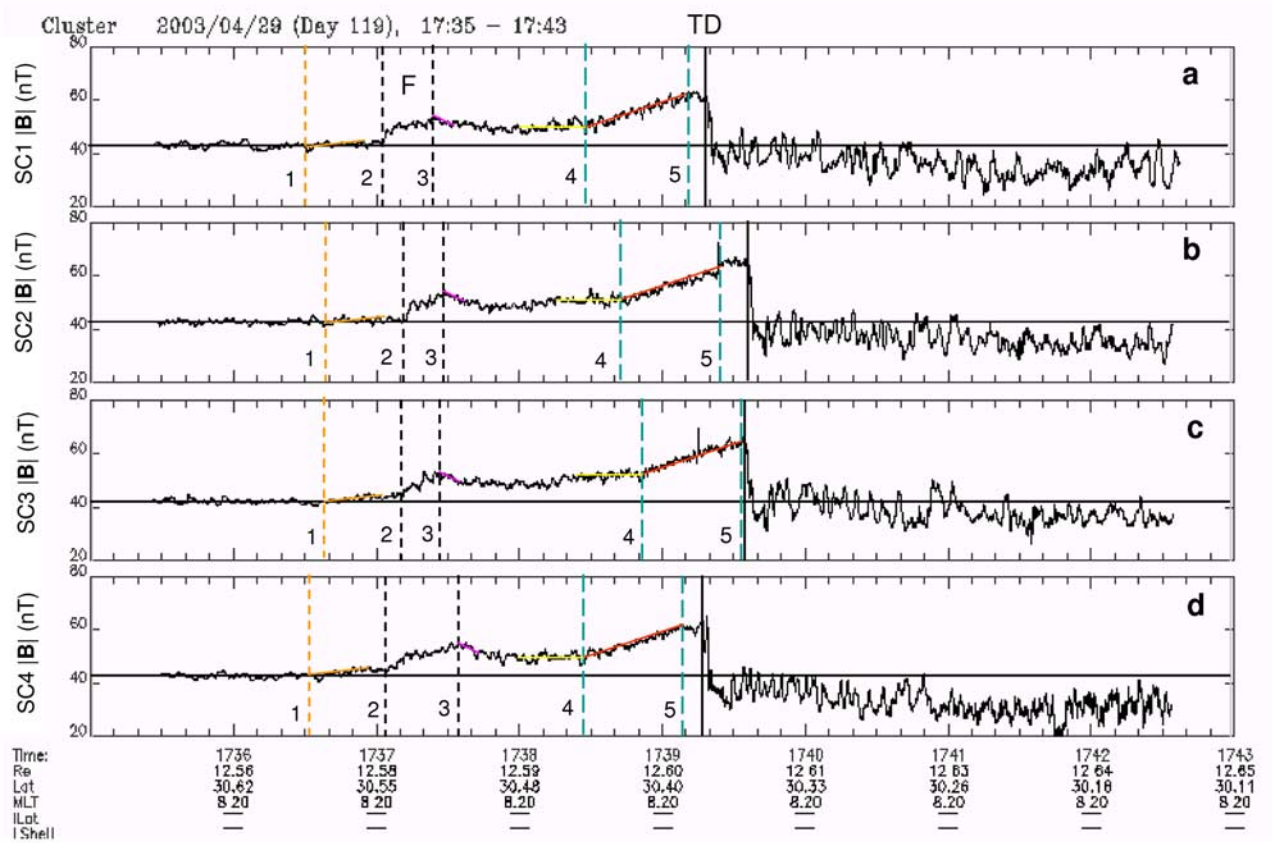

Figure 5. The magnitude of the magnetic field measured by each of the four Cluster satellites. The beginning of the fast wave and the TD are highlighted by the dashed line 2 and the solid line, respectively. Dashed line numbering is the same as in Figure 3. The slow-mode structure is marked by dashed lines 4 and 5, with the beginning time defined by the change in slope, indicated by the yellow and red overlay lines.

[19] Assuming that features like the TD or the fast shock have locally planar surfaces that move at nearly constant speed we can estimate their velocities and propagation directions using the triangulation method of *Russell et al.* [1983; see also *Knetter et al.*, 2004], namely,

$$\mathbf{R_3} \bullet \mathbf{n} = V_n T_3, \tag{1}$$

where $\mathbf{R_3}$ is a 3 × 3 matrix whose components are the separation vectors ($\mathbf{r_{13}}$, $\mathbf{r_{23}}$, $\mathbf{r_{43}}$) with respect to the reference spacecraft 3, $\mathbf{n}$ is the unit vector in the direction of propagation, V_n is the velocity of propagation, and T_3 are the separation times (t_{13}, t_{23}, t_{43}), relative to the reference spacecraft. Note that while Cluster 4 made first contact with the TD, Cluster 1 was first to observe the fast shock. This indicates that the TD and fast shock had slightly different propagation directions. Using the starting times for each feature listed in Table 2, we first determined the velocity of the TD to be 188 km/s in a GSE direction of (−0.9986, 0.0197, −0.0494). This direction is 17.4° from the TD normal determined from a minimum variance analysis of Cluster 1 data. Similarly, the velocity of the fast shock feature was determined to be 456 km/s in a GSE direction of (−0.9690, 0.2262, −0.1008), or 6.7° from the TD minimum-variance normal and 12.3° from the triangulated TD normal. The fast mode wave propagated in a direction almost orthogonal to the magnetic field. Using Cluster 1 measurements, the angle of propagation to the magnetic field at the beginning of the wave was 83.6°, while at the maximum amplitude of the wave the angle to **B** was 89.7°. Further justification for our planar wavefront assumption is presented below.

[20] The rise in |**B**| associated with the fast shock (after line 2) has different durations at the four spacecraft. Starting at each line 3, the magnitude decreases at the same rate and duration at each spacecraft, highlighted by the pink overlay. The times for line 3 are given in Table 2. We determined the velocity of this feature from triangulation to be 405 km/s in a GSE direction (−0.4081, −0.8333, 0.3733). This velocity is comparable in magnitude to that of the fast shock but propagates in a very different direction. We label it *R*, and present arguments in section 5 that suggest it is the signature of a fast rarefaction wave reflected from the magnetopause.

Table 2. Event Start Times in UT

Event	Cluster 1	Cluster 2	Cluster 3	Cluster 4
Directional discontinuity	1739:18.4	1739:36.5	1739:35.0	1739:17.0
Fast wave	1737:03.1	1737:12.1	1737:10.8	1737:04.5
Reflected fast wave	1737:23.9	1737:28.4	1737:27.1	1737:34.5
Slow-mode structure	1738:27.6	1738:42.7	1738:51.2	1738:26.9

[21] The increase in $|\mathbf{B}|$ that occurred between dashed lines 4 and 5 just before the TD arrival was of similar duration at all four spacecraft. This increase came after a density enhancement and occurred during an interval where the density is nearly constant, i.e., decreasing relative to the upward trend (Figure 3b). Recall that an increase in $|\mathbf{B}|$ with a corresponding decrease in density is a characteristic of a slow-mode wave. Red lines, with the same slope and duration, follow the increases in $|\mathbf{B}|$ at each spacecraft. Yellow lines highlight the nearly constant values before the interval. The start times (Table 2) at each satellite are taken to be when the yellow and red lines intersect. The velocity determined from triangulation is 152 km/s in a GSE direction of (−0.9303, −0.1847, −0.3168). The structure's velocity was less than that of the plasma (Figure 3d) and at significant angles to those of both the plasma and TD. Finally, we note that immediately after the TD passage, the magnetic field's fluctuation level increased significantly.

[22] Figure 6 presents ion spectra and velocity moments measured by the CIS CODIF instrument on Cluster 4. Figures 6a–6d show the total, parallel, perpendicular, and antiparallel H^+ differential ion fluxes. Figures 6e–6h show the X, Y, and Z components of the ion velocity and the bulk speed. The times of arrival for the TD and the fast shock are marked with the solid line and dashed line 2, respectively. The dashed line 1 marks the beginning of an increase in negative V_Y and $|\mathbf{V}|$ (Figures 6f and 6h). It was placed at the same spacecraft-relative UT position as the dashed line 1 in Figures 5d and 3b. The velocity increase between the start of the fast shock (dashed line 2) and the arrival of the TD was primarily in negative V_X, with help from negative V_Y increases. The ion velocity's magnitude was 251 km/s before the TD crossing, and it then fell to 202 km/s (horizontal dotted lines in Figure 6h), with X components before and after of 175 and 200 km/s. This compares well with the TD velocity of 188 km/s in the X direction estimated above from triangulation, consistent with the TD being convected with the flow normal to its surface. Note that the sharp decrease in negative V_Y and the decrease toward zero in V_Z at the TD place the final ion velocity direction nearer to that of the TD. The perpendicular ion spectra indicate that heating began at the start of the fast shock (highlighted by the oval in Figure 6c). This was also seen at Cluster 1 (Figure 3f). Intensifications of the parallel and perpendicular fluxes at the TD in Figures 6b and 6c reflect the large increase in density of the incoming solar wind stream diverting around the magnetopause. The increase in the ion flux parallel to the new direction of $\mathbf{B}$ is dominated by negative Y and positive Z components.

[23] We compared the three components of the velocity measured by CIS CODIF with those calculated from the $\mathbf{E} \times \mathbf{B}$ drift. The agreement (not shown) was very good, as expected, for the X and Y components, establishing that the velocity is indeed convective. A difference in the Z components may be attributed to a field aligned component of velocity. The negative X and Y components with the positive Z component is consistent with tailward flow being diverted away from the subsolar magnetopause to the location of Cluster on the dawnside and in the northern hemisphere [*Spreiter and Alksne*, 1969].

[24] As estimated by triangulation, the fast shock propagated primarily in the $-X$ direction. In the rest frame of the plasma, a plane wave with the principal $\mathbf{E}$ and $\mathbf{B}$ components in the $+Y$ and $-Z$ directions, respectively, causes an increase in negative V_X, which was observed at the time of the fast shock (Figure 6e). The fast shock should be recognizable as a change from the background in these components of $\mathbf{E}$ and $\mathbf{B}$. Figure 7 displays the ion density and the three components and magnitudes of $\mathbf{E}$ and $\mathbf{B}$ in the proximity of the fast shock, which is highlighted by dashed lines 2 and 3. The increases in the magnitudes (solid arrows) related to the fast shock are dominated by changes in $+E_Y$ and $-B_Z$ (dashed arrows). Negative E_X also increases (Figure 7c) which, in turn, is consistent with the increase seen in negative V_Y (Figure 6f).

[25] Currents associated with the fast shock and TD were determined from $\nabla \times \mathbf{B}$ using the curlometer tool [*Dunlop et al.*, 2002]. Figures 8a–8c show the Z, Y, and X components of calculated currents on a scale that emphasizes the fast shock (red circle). The scale of Figure 8d is expanded to capture the current's peak in the Y component through the TD passage. A measure of accuracy can be obtained by changing the order of the spacecraft in the curlometer calculation. Variations between such calculations were ∼15% of the magnitudes of currents in the fast shock. A second measure of accuracy is $\nabla \bullet \mathbf{B}$ (which should be zero). Values of $\nabla \bullet \mathbf{B}$ were variable, but at levels of ∼30% of the currents in the fast shock and <10% of those in the TD. Both tests indicate that the current determination is valid. J_Y associated with the fast shock was first positive, >3 nA/m^2, and then slightly negative, following variations in $|\mathbf{B}|$ (Figure 3g). Significant variations also appeared in J_Z. Within the TD current sheet J_Y and J_Z, approached −30 and −5 nA/m^2, respectively. Using the duration of the J_Y signature in the TD (30 s; Figure 8d) and the triangulated velocity of 188 km/s, we obtain a current layer thickness of ∼0.9 R_E.

4.3. Simulation Results

[26] Solar wind and IMF conditions for the observed discontinuity were altered slightly for the global MHD simulation. To simplify implementation of changes at the upstream simulation boundary in the solar wind and insure that the imposed discontinuity was a TD, the IMF B_X and the solar wind velocity components V_Y and V_Z were all set to zero. Consequently, the other components of the IMF were increased to approximate the same magnetic pressure. In the simulation the Earth's magnetic dipole axis was positioned parallel to the Z axis. IMF values used in the simulation where taken from GSM coordinates so as to maintain the correct IMF clock angle relative to the Earth's magnetic dipole field. The observed GSM values for IMF B_Y and B_Z were −1.4 and −10.1 nT before and −6.0 and 4.5 nT after the TD. These components of the IMF, as well as the plasma density, and temperature were adjusted to maintain force balance across the simulated TD to satisfy the Rankine-Hugoniot relations. Therefore, initial conditions used in the simulation were n = 3.0 cm^{-3}, V_X = 530 km/s, $T_i = T_e$ = 180,000 °K with B_Y = −1.5 nT and B_Z = −11.0 nT. The upstream TD conditions were n = 7.66 cm^{-3}, B_Y = −7.0 nT, and B_Z = 4.0 nT with V_X, T_i, and T_e unchanged. ISM was run for two hours simulation time (ST) to establish the steady state magnetosphere configuration appropriate for initial solar wind conditions. The final solar wind conditions were

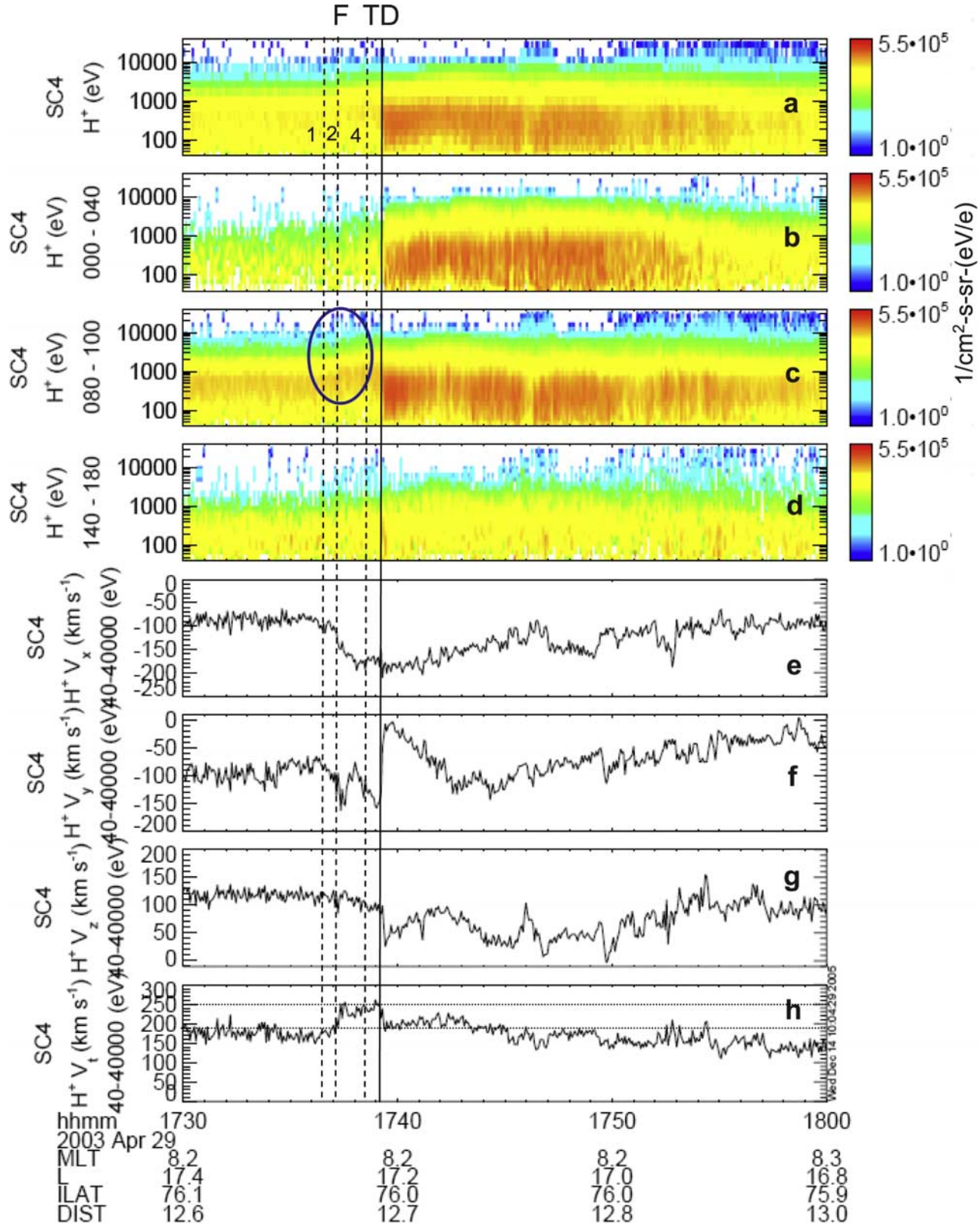

Figure 6. Cluster 4 ion spectrogram and velocity moment data from CIS-CODIF. (a–d) Proton energy spectrograms showing the total energy flux, the parallel component, the perpendicular component, and the antiparallel component. (e–h) The three components and magnitude of the proton velocity moments. Dashed line numbering is the same as in Figure 3.

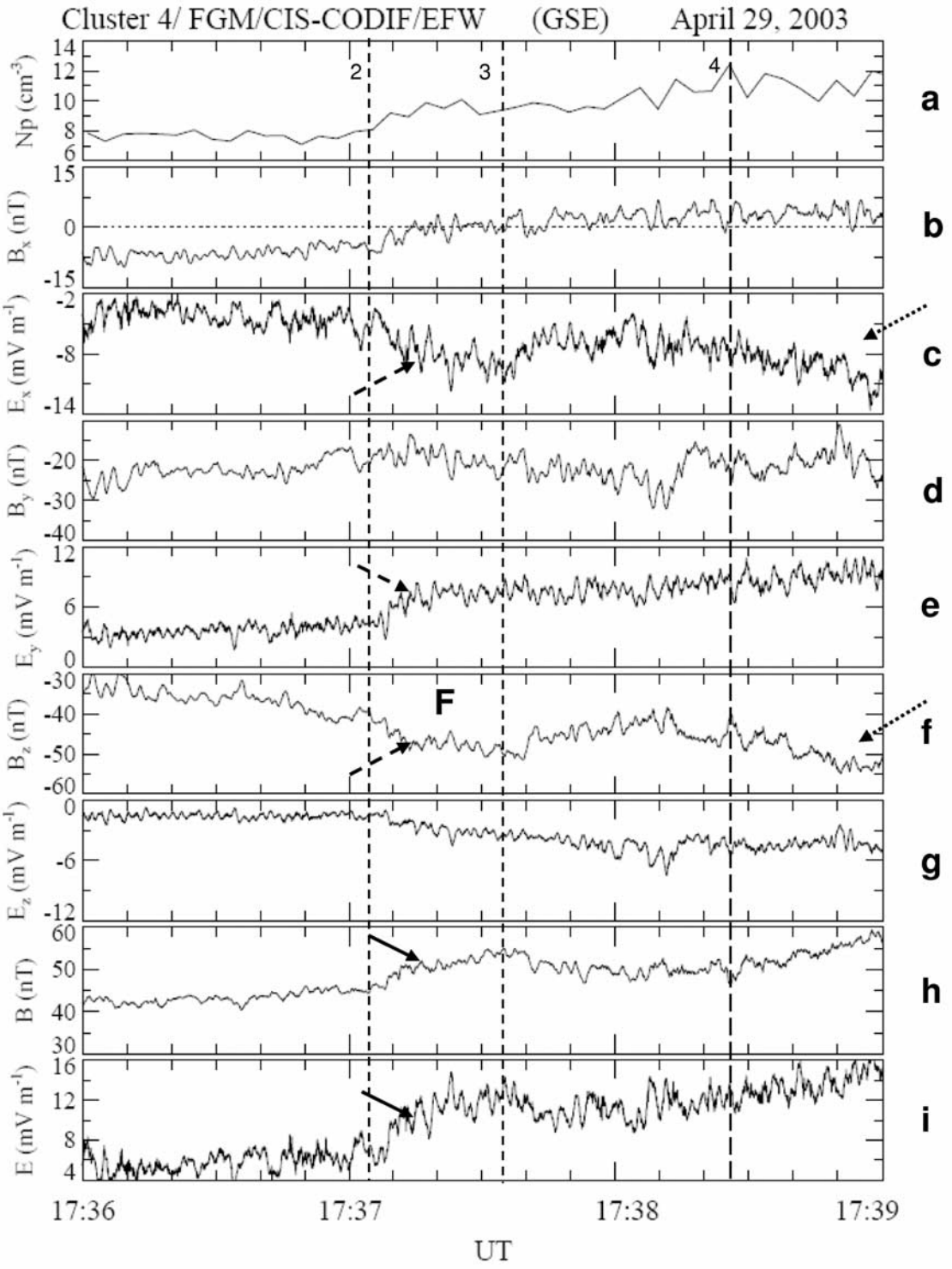

Figure 7. High-resolution measurements from Cluster 4 of the magnetic and electric field magnitudes and components as well as the proton density from 1736 to 1739 UT. The solid arrows point to the increase in magnitude of both **B** and **E**, associated with the fast wave. The dashed arrows indicate that the principal contributors to these changes are B_Z, E_Y, and (to a lesser degree), E_X. The dotted arrows indicate that the principal contributors to the changes in $|\mathbf{B}|$ and $|\mathbf{E}|$ in the slow-mode structure are B_Z and E_X. Dashed line numbering is the same as in Figure 3.

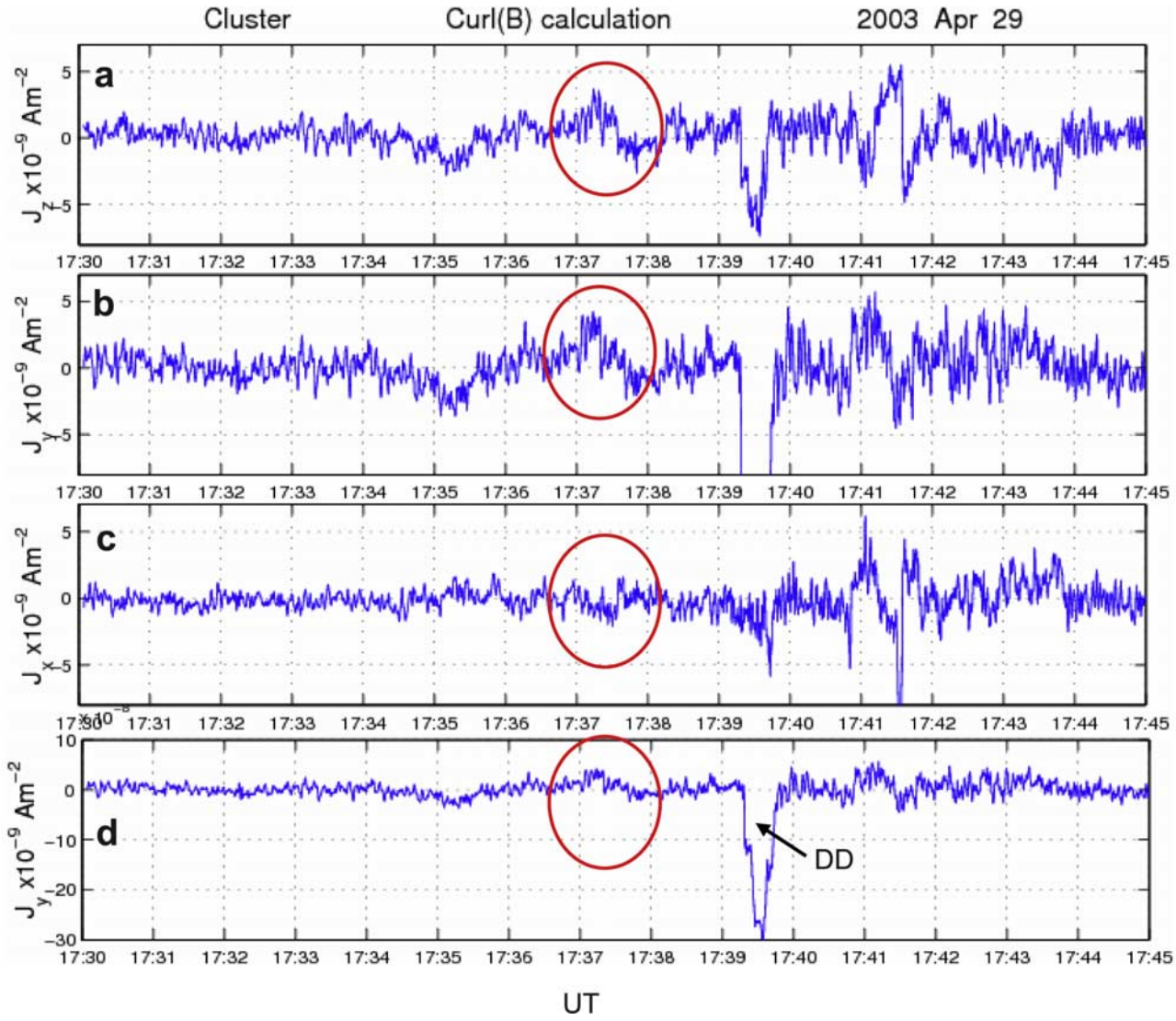

Figure 8. Current determined from the curl B based on magnetic field measurements from the four Cluster spacecraft. (a–c) The three components of **J** in GSE coordinates. (d) The *Y* component with a scale set to resolve the maximum current in the directional discontinuity (DD).

then changed instantaneously at the sunward boundary of the simulation grid. The width of the TD as it appeared on the simulation grid was 2 R_E (~30 s convection time past a fixed point) and maintained that width until it impacted the bow shock. Unfortunately, when the discontinuity was introduced onto the grid some oscillations developed and propagated ahead of the simulated TD. The oscillations primarily appear in the plasma temperature. When comparing the observations with our simulation results the appropriate location of the Cluster constellation relative to the magnetic dipole axis in the simulation is the SM coordinate position of (6.0, −9.1, 6.5 R_E).

[27] Figure 9 plots variations of 8 simulated quantities as functions of time along a line parallel to the *X* axis (Y = −9.1 and Z = 6.5 R_E) passing through the approximate location of Cluster. The *X* coordinate of Cluster is noted by the vertical line. The magnitudes of simulated quantities are coded as indicated by adjacent color bars. Figures 9a and 9b show variations of B_Y and V_X, while Figures 9c and 9d depict variations of |**B**| and n. The magnetopause and bow shock are marked by blue arrows in Figures 9a and 9c, respectively. The orange line in Figure 9a highlights a fast shock starting from the bow shock and progressing to the magnetopause, carrying a portion of the density increase (Figure 9d) as predicted by *Wu et al.* [1993]. The passage of the DD is highlighted by the black line in Figure 9a. Pressure balance was maintained across the DD (dashed line in Figure 9g) until after it passed the Cluster location (vertical line in each panel of Figure 9). This is consistent with the conclusion from the observations that the DD remained a TD as it passed Cluster.

[28] The fast shock emerged from the bow shock at the time of impact of the density increase and the TD. The bow shock simultaneously started to move earthward. We note in passing that the change in density rather than magnetic field initiates the fast shock. In other simulations (not shown) where changes in the IMF orientation or magnitude were not accompanied by changes in solar wind density, no fast

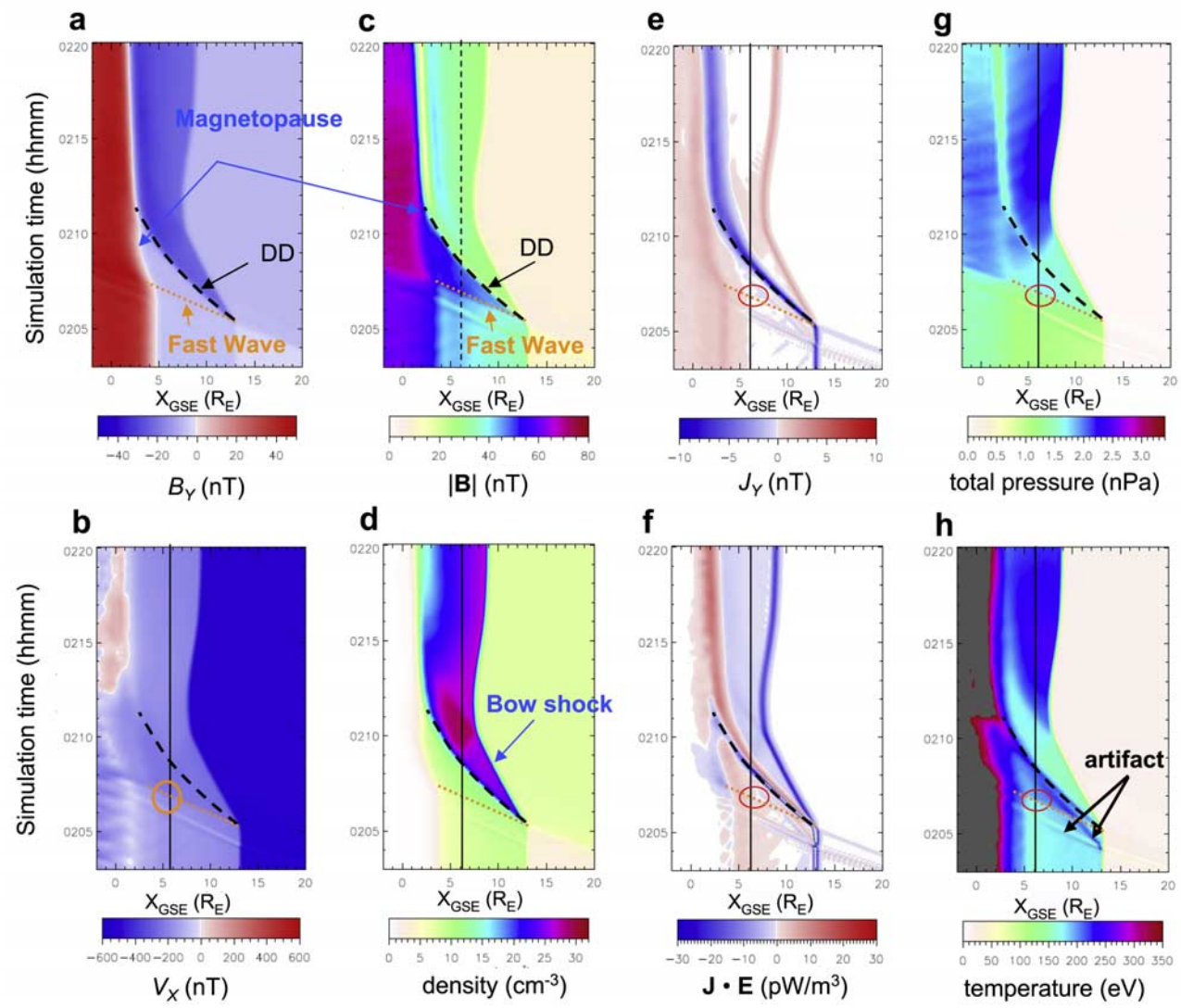

Figure 9. The X variation versus simulation time of eight quantities from the ISM MHD simulation. The Y and Z coordinates are -9.1 and 6.5 R_E, respectively. These coordinates, and $X = 6.0$ R_E (vertical line), are the SM coordinates of Cluster at the time of the DD. The DD, the fast wave, and the reflected fast wave are highlighted.

shock was launched at the time of impact with the bow shock. The change in dynamic pressure carried by the fast shock caused the first earthward motion of the magnetopause (Figure 9c). In this way the new equilibrium positions of the bow shock and magnetopause are established. Over the fast-wave interval both J_Y (Figures 8a and 9e) and E_Y (Figure 7e) were positive. Thus, **J** • **E** was weakly positive (red circle in Figures 9f), indicating that electromagnetic energy dissipates to heat ambient particles. This is confirmed by the increase in temperature at the fast shock (red circle in Figure 9h). We also observe an increase in total pressure at the fast shock crossing (red circle in Figure 9g).

[29] As previously noted, a temperature-oscillation artifact propagated ahead of the TD in the simulated solar wind. This oscillation interacted with the bow shock to launch a fast wave and a slower-moving structure into the magnetosheath before the TD reached it. Its effects are best seen in **J** • **E** and temperature variations in Figures 9f and 9h. This artifact should not be regarded as representing actual conditions. However, the slower-moving wave approaches the DD soon after it crosses the fast shock and merges with the DD before reaching the position of Cluster (vertical line). This tends to obscure processes occurring just downstream of the DD until it is overtaken by the DD. This prevents us from tracking the observed slow-mode like structure (Figure 4), in the simulation prior to its appearance at Cluster's position.

[30] The fast shock planar structure while approaching the magnetopause is highlighted by black arrows in Figures 10a (density) and 10e (J_Y). Scales were chosen to emphasize density and current values in the fast shock, while allowing them to saturate in the DD. Simulated values for J_Y in the fast shock and DD reached $\sim$0.4 nA/m^2 and -9 nA/m^2, respectively. These have the proper signs but are of significantly lower magnitudes than the observed 5 nA/m^2 and

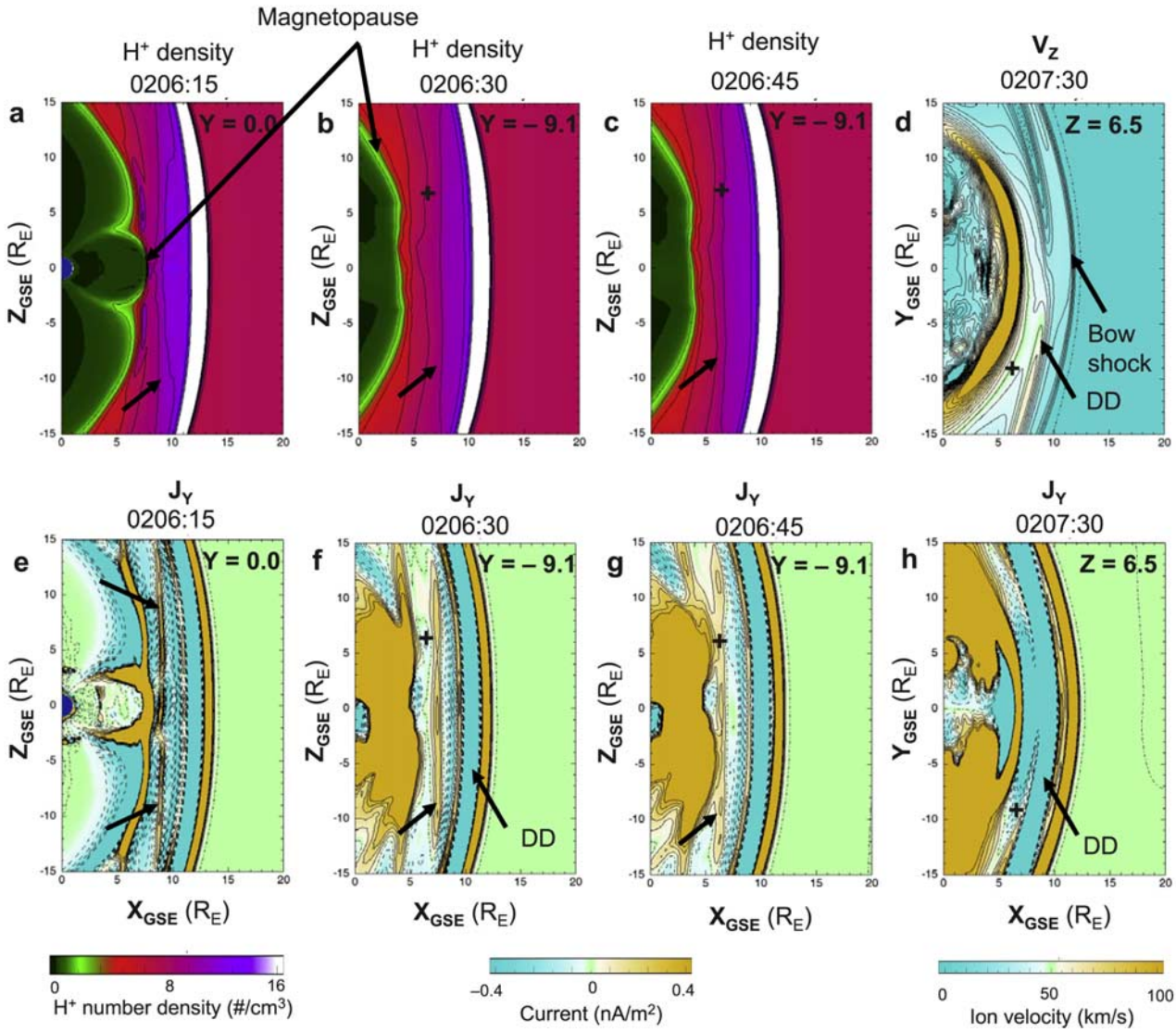

Figure 10. Spatial variations of density and J_Y at different simulation times and different XZ planes. (a, e) The plane at $Y = 0$, showing the approach of the fast wave to the nose of the magnetopause. (b, c, f, g) The plane at $Y = -9.1\ R_E$, showing the fast wave crossing the Cluster position (+). (d, h) Variations of V_Z and J_Y in the XY plane at $Z = 6.5\ R_E$ at a time when the slow-mode structure was passing Cluster.

-30 nA/m^2 (Figure 8). The thickness of the simulated DD current layer is $\sim$1.6 R_E and partially accounts for the lower maximum amplitudes of J_Y. Figures 10b and 10f and Figures 10c and 10g show the same quantities 15 and 30 s later, but in the XZ plane at the Y simulation coordinate of Cluster. The fast shock crossed the simulated location of Cluster (+) between these two times. At both times it had already reached the subsolar magnetopause. The fast shock maintained its locally planar configuration even after its first impact with the magnetopause. However, the DD clearly appears curved subsequent to its interaction with the bow shock. Note the positive J_Y at the wavefront. The simulation also showed that $\mathbf{J} \bullet \mathbf{E}$ is positive along the wavefront, indicating that the wave is a source of energy for heating particles. Initially, the simulated V_X in the magnetosheath was -176 km/s. The simulated fast shock propagated inward at 583 km/s, and the velocity between the fast shock and the modified bow shock was -253 km/s. This compares with measured plasma velocities downstream of the fast shock of -188 km/s and -265 km/s upstream of the fast shock. The observed fast shock velocity obtained via triangulation was 456 km/s.

[31] There is a second band of current in the $+Y$ direction between the fast shock and the bow shock on the downstream side of the DD. This second region of $J_Y > 0$ remains close to the DD (Figures 10e–10g). Figures 10d and 10h show variations of V_Z and J_Y in the XY plane at $Z = 6.5\ R_E$ at 0207:30 ST. The positive J_Y is near Cluster, which is in a region of decreased upward velocity. The positive J_Y disappeared in regions closer to the subsolar magnetopause, where it had been overtaken by the faster moving DD (Figure 10h). We noted above that the slower artifact

temperature wave (Figures 9f and 9h) did not reach the position of Cluster before was overtaken by the DD. It cannot be the cause of variations near the Cluster position at 0207 ST.

5. Discussion

[32] The interaction of a TD and an accompanying density increase with the bow shock launches a fast shock that propagates toward the magnetopause faster than the transmitted DD, carrying a portion of the density increase [*Völk and Auer*, 1974; *Wu et al.*, 1993]. Upon its arrival at the magnetopause, the fast shock causes this boundary to begin moving toward a new equilibrium position closer to Earth. The interaction of the fast shock with the magnetopause launches a transmitted fast shock into the lower-density magnetosphere and a reflected rarefaction wave back toward the bow shock [*Grib et al.*, 1979; *Samsonov et al.*, 2007]. This chain of events is represented schematically in Figure 4c. Measurements from the four Cluster spacecraft on 29 April 2003 and simulations characterize the fast shock, the reflected rarefaction wave, and the DD in the magnetosheath (which we showed to be a TD as it passed Cluster), initiated by a factor of 2.5 jump in the solar wind density and a magnetic field rotation of 122°. Cluster also observed a structure just downstream of the TD that was traveling at a slower speed. The three following subsections compare observations with theoretical expectations and MHD simulation results to discuss the properties of the fast shock, the TD, and other observed features. The other features include a reflected rarefaction wave from the magnetopause, a weaker fast shock from an initial smaller density change observed at Wind, and the slower-moving structure located just before the TD.

5.1. Fast Shock

[33] Changes in plasma density and $|\mathbf{B}|$ associated with fast shocks occur in phase. Cluster 1 data streams indicate that, beginning at 1736:11 UT, this condition was met (Figure 3b and 3e). In the plasma's rest frame fast waves propagate at the magnetosonic speed. As they steepen into a shock, the shock speed will exceed the magnetosonic speed of the downstream unshocked plasma. Figures 11a–11d show the sound ($\mathbf{C_S}$), Alfvén (V_A), magnetosonic (V_{MS}) and the bulk speeds for the interval 1730 to 1750 UT derived from Cluster 1 FGM and CIS data. Figures 11e–11g display the corresponding sonic, Alfvénic, and magnetosonic Mach numbers. Figures 11h and 11i show the proton beta and the quantity ($T_\perp/T_\parallel - 1 - 1/\beta_\perp$) which determines the mirror-mode stability of the magnetosheath plasma (>0: unstable). From the latter plot we see that magnetosheath plasma was mirror-mode stable prior to the TD's passage and unstable thereafter. Triangulation analysis determined that the velocity of the fast shock was 456 km/s in a GSE direction (−0.9690, 0.2262, −0.1008), ∼89.7° from the direction of **B**. Vector subtraction of the measured, unshocked downstream ion velocity of 188 km/s in a GSE direction (−0.5594, −0.5860, 0.5860) yields a fast-shock velocity in the plasma rest frame of 428 km/s in a direction (−0.7869, 0.4979, −0.3642), ∼80.4° from the direction of **B**. At the start of the event the $\mathbf{C_S}$ and V_A were 288 and 327 km/s, respectively. The resultant magnetosonic velocity for perpendicular propagation is 435 km/s. For nonperpendicular propagation the dispersion relation for the fast and slow modes is

$$V^2 = \frac{\omega^2}{k^2} = \frac{1}{2}\left\{(V_A^2 + \mathbf{C}_\mathrm{S}^2) \pm \sqrt{(V_A^2 + \mathbf{C}_\mathrm{S}^2)^2 - (4V_A^2\mathbf{C}_\mathrm{S}^2\cos^2\theta)}\right\}, \tag{2}$$

where V is the phase velocity of the wave and θ is the angle between the wave vector **k**, and **B**. Plus and minus signs refer to fast and slow-mode waves, respectively [cf. *Kivelson and Russell*, 1995]. With $\theta = 80.4°$, the fast-mode speed in the unshocked downstream plasma is 434 km/s, which is very close to the measured shock velocity of 428 km/s, estimated in the plasma's rest frame. That the shock velocity is not higher than the fast mode velocity may be attributed to errors in both calculations and to the weakness of the shock.

[34] Simulation results shown in Figure 10 indicate a planar fast wavefront. The conservation of momentum equation and Ampere's law for a plane wave whose perturbation **b** is small compared to the background **B** is

$$\rho\left[\frac{\partial}{\partial t}\mathbf{v} + \mathbf{v}\cdot\mathrm{grad}\ \mathbf{v}\right] = -\mathrm{grad}(\delta\mathbf{p}) + \mathbf{J}\times\frac{\mathbf{B}}{\mu_o} = -\mathrm{grad}(\delta\mathbf{p}) + (\mathrm{curl}\ \mathbf{b})\times\frac{\mathbf{B}}{\mu_o}, \tag{3}$$

where ρ is the mass density, **v** is the wave velocity, and $\delta\mathbf{p}$ is the pressure perturbation associated with the wave [see *Kivelson and Russell*, 1995]. The wave variations in **E** are strongest in $+Y$ and weaker in $-X$, while those in **b** are strongest in the $-Z$ and weaker in $+X$ (see Figure 7). The combined $+E_Y$ and $-b_Z$ variations produce the observed velocity increase in the $-X$ direction. Note that a current was observed in the simulation in the $+Y$ direction along the fast wavefront (Figure 9e and Figure 10). The Y component of curl **b** is $(d/dz)(b_X) - (d/dx)(b_Z)$. Since the change in b_Z in the X direction is negative and that is the dominant component of the variation, we expected a current in the $+Y$ direction. In the fast shock the current density derived from Cluster magnetic field measurements was $J_Y \approx +3$ nA/m^2 (Figure 8). Positive J_Y crossed into **B** gives a force in the $-X$ direction, which is the same direction as the negative pressure gradient term. Thus the **J** x **B** force must be balanced by the inertial term (ρ [$(\partial/\partial t)(\mathbf{v})$ + **v** • grad **v**]) of the force-balance equation. In the simulation the required negative $(\partial/\partial t)(v_X)$ appears as a change in color across the fast shock (inside the orange circle in Figure 9b). A similar change in the observed $-V_X$ is seen in Figure 6b, although some of that variation may have been spatial. The X component of **v** • grad **v** is also negative.

[35] A positive **E** • **J** indicates that electromagnetic field energy is available to heat particles. The simulated E_Y and J_Y are both positive in the fast shock (Figure 9f). A positive E_Y was measured, and we have determined a positive J_Y from the components of curl **b** and the Curlometer analysis (Figure 8). We noted above that ion heating occurred as the fast shock passed (Figure 6c). However, this heating was

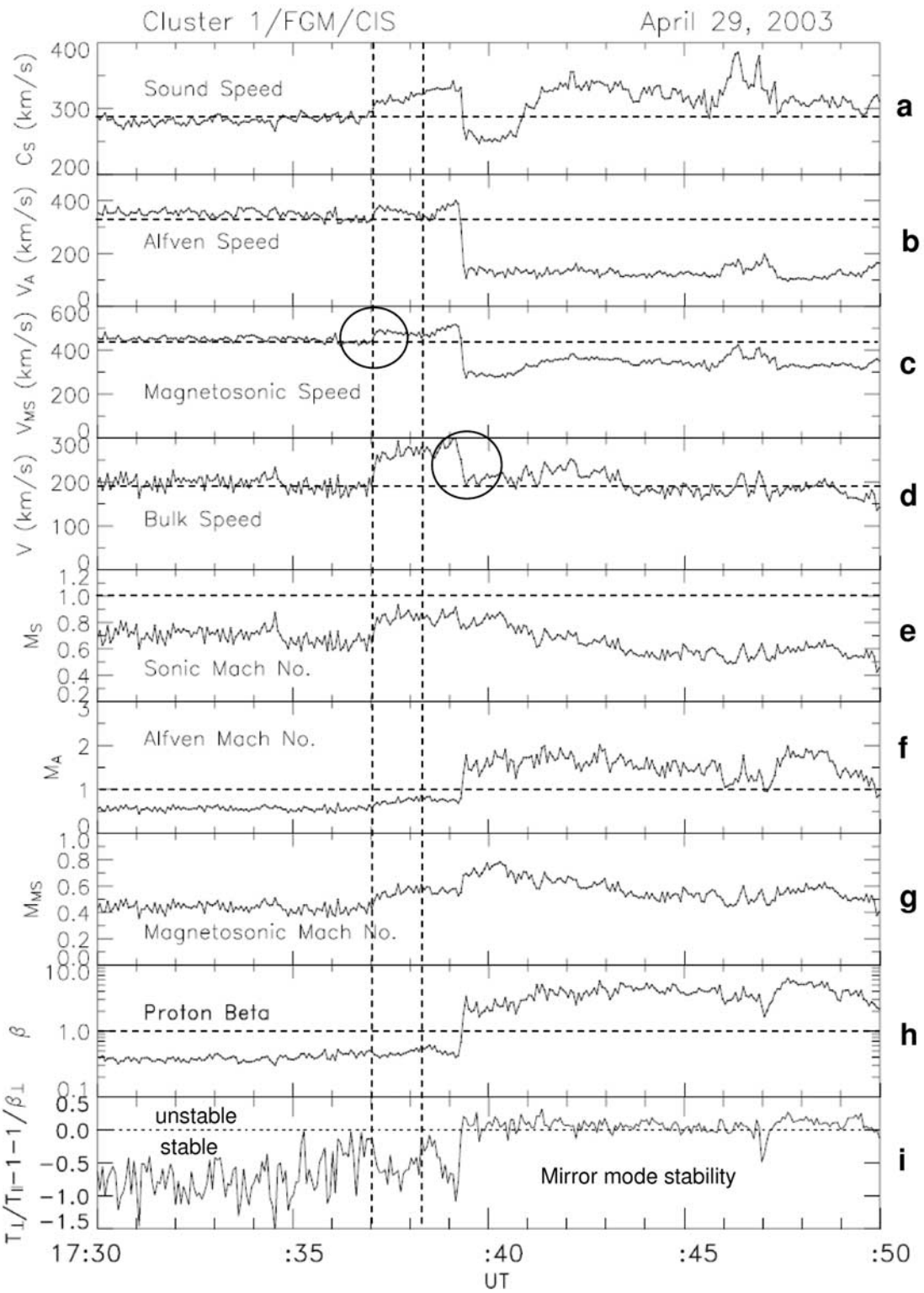

Figure 11. Variations of the sound, Alfvén, magnetosonic, and bulk speeds; the sonic, Alfvén, and magnetosonic Mach numbers; the proton beta; and the mirror mode stability criteria calculated from the Cluster observations.

much weaker than the strong perpendicular acceleration observed in transition layers adjacent to the fast rarefaction wave and the strong parallel acceleration within that wave [*Maynard et al.*, 2007]. In that case nonlinear terms in the Korteweg–de Vries equation were probably responsible for the perpendicular acceleration. Most likely the parallel acceleration in their rarefaction wave can be ascribed to ambipolar electric fields.

5.2. Tangential Discontinuity

[36] As noted above, the observed discontinuity maintained the characteristics of a TD during its passage across the bow shock and magnetosheath to the location of Cluster. The triangulated velocity of the TD was 188 km/s, with GSE components of (−187.8, 3.7, −9.3) km/s (almost totally in the $-X$ direction). V_{TDX} was almost halfway between the ion velocity downstream and upstream X components of −175 and 200 km/s, respectively. The difference velocities on each side of 12.8 and −12.2 km/s pointed toward the plane of discontinuity, indicating that the TD was being compressed as it propagated inward. High-resolution magnetic and electric field data from Cluster 4 are plotted in minimum variance coordinates (i, j, k, where k is the normal direction) in Figure 12. Minimum variance analyses on two nested intervals (Table 1) yielded nearly the same normal, which was within 4.1° of the triangulated velocity direction. In panels c and e the red traces are $-\mathbf{V_{TD}} \times \mathbf{B}$, and the dashed traces near zero are the differences between the measured electric field and $-\mathbf{V_{TD}} \times \mathbf{B}$, which is the electric field in the rest frame of the discontinuity ($\mathbf{E_R}$). $E_{R\,j}$ (and E_{Ri}) is nearly constant, of the order of −1 mV/m (0 mV/m) downstream and 0.6 mV/m (1 mV/m) upstream. Both components vanish in the discontinuity, as required for the tangential electric field in a TD. The k component of the velocity calculated from the cross product of $\mathbf{E_R}$ and $\mathbf{B}$ is 17 km/s downstream and −24 km/s upstream. They point toward the discontinuity surface and compare favorably in magnitude with the values for the differences between X_{GSE} velocity components established using CIS data. The magnitude of the plasma bulk velocity is larger than the velocity of the TD (dashed line in Figure 11d) allowing slippage along the discontinuity.

[37] As the TD approached the magnetopause in the magnetosheath it was compressed. Along with a growing curvature in the surface of discontinuity resulting from the slower velocity of the TD in the magnetosheath compared to that in the solar wind, this compression may eventually have lead to the TD evolving into a RD, accompanied by magnetic merging within the magnetosheath [*Maynard et al.*, 2002, 2007; *Phan et al.*, 2007]. However, as noted above when the discontinuity passed Cluster it still maintained the characteristics of a TD.

[38] An interesting aspect of Cluster's passage through the TD is the change in the fluctuation/turbulence level of the magnetosheath. This shocked solar wind region is known to be turbulent, in general. Temperature anisotropies can give rise to wave instabilities, principal among which are drift mirror mode waves and ion cyclotron waves [*Fairfield and Ness*, 1970; *Tsurutani et al.*, 1982]. The mirror instability is a nonoscillatory compressional mode whose frequency is purely imaginary and whose variations drift with the plasma [see *Hasegawa*, 1975]. Before the fast shock reached Cluster and in the transition region between the fast shock and the TD the level of fluctuations in $|\mathbf{B}|$ was small (see Figure 4). After the TD passed Cluster the amplitudes of fluctuations increased significantly. In this region the bulk flow turned super Alfvénic (Figure 11f) as β (Figure 11h) transitioned from low to high values. If the quantity $(T_\perp/T_\parallel - 1) - 1/\beta_\perp$ plotted in Figure 11i is negative (positive), the region is stable (unstable) to the mirror mode instability. Large values of β reduced the second term making it easier for mirror-mode waves to grow upstream of the TD in the magnetosheath. The conditions upstream of the TD in the solar wind, namely higher density (by a factor of about 2.8), lower Tp (1/2) and smaller $\mathbf{B}$ (2/3) (Figures 1a, 1c, and 1e) are instrumental in this but are not enough to account for the observed β increase of more than an order of magnitude. Evidently the jumps were enhanced at the bow shock, most particularly the density. The ensuing high proton β after the TD favors the destabilization of the mirror mode and local generation of the fluctuations. The absence of mirror mode waves in the magnetosheath downstream of the TD made it easier to distinguish the observed fast and slow-mode structures.

5.3. Other Features

[39] Times of maximum $|\mathbf{B}|$ after the beginning of the fast shock at the four spacecraft differed (line 3 in each panel of Figure 5 and the third line of Table 2). We investigated the possibility that the subsequent decrease in $|\mathbf{B}|$ could be the signature of a rarefaction wave reflected from the magnetopause interaction. The bulk velocity was subtracted from the triangulated velocity of 405 km/s to approximate the wave's velocity in the plasma rest frame of 333 km/s in a GSE direction of (−0.0465, −0.5785, 0.8143). The angle between the rest frame velocity and $\mathbf{B}$ was 52.9°. For this propagation angle to $\mathbf{B}$ the fast mode velocity was 326 km/s which compares favorably. Away from the curved subsolar magnetopause the angle of incidence should equal the angle of reflection. Qualitatively, we expect that for such a wave to reach the GSE location of Cluster 3 (7.6, −6.8, 6.4) R_E the reflection surface must lie a magnetopause location nearer to the equator and to noon. The simulation indicates that the fast shock intercepted the subsolar magnetopause, ∼ 30 s before its detection by Cluster. To this we add the order of 30 s after the initial observation of the fast shock for the decrease to start to provide a significant propagation time from the magnetopause reflection point to Cluster. Propagation is primarily in the +Z and −Y directions. This places the reflection point several R_E below and toward the Earth-Sun line from the location of Cluster, which was then on the dawn side of the cusp. The complex magnetopause configuration near the cusp renders a more accurate determination of the reflection point impractical.

[40] To consider the structure as a rarefaction wave, we must regard a constant density as a decrease relative to the upward trend initiated at the time of line 1. Similar logic is applied in the slow wave discussion below. The upward trend in density (Figure 3b) is clear. But what is its cause? Information about the TD's interaction with the bow shock cannot propagate quicker than the fast shock. Figure 13 expands the density, velocity, temperature dynamic pressure and the magnitude of $|\mathbf{B}|$ observed at Wind in the 2-min interval centered on the TD (vertical dashed line). Note that the density, velocity and dynamic pressure increase occurred in two steps (highlighted by the vertical lines 1 and 2), with the second step being the larger. This opens the possibility that the smaller first step could have launched a weak fast shock that arrived ahead of the main shock thereby initiating the upward trend in density. We already noted that the density increase was accompanied at all four spacecraft by a gentle rise in $|\mathbf{B}|$, starting at line 1 in Figure 5. Because variations were small, it is impossible to identify

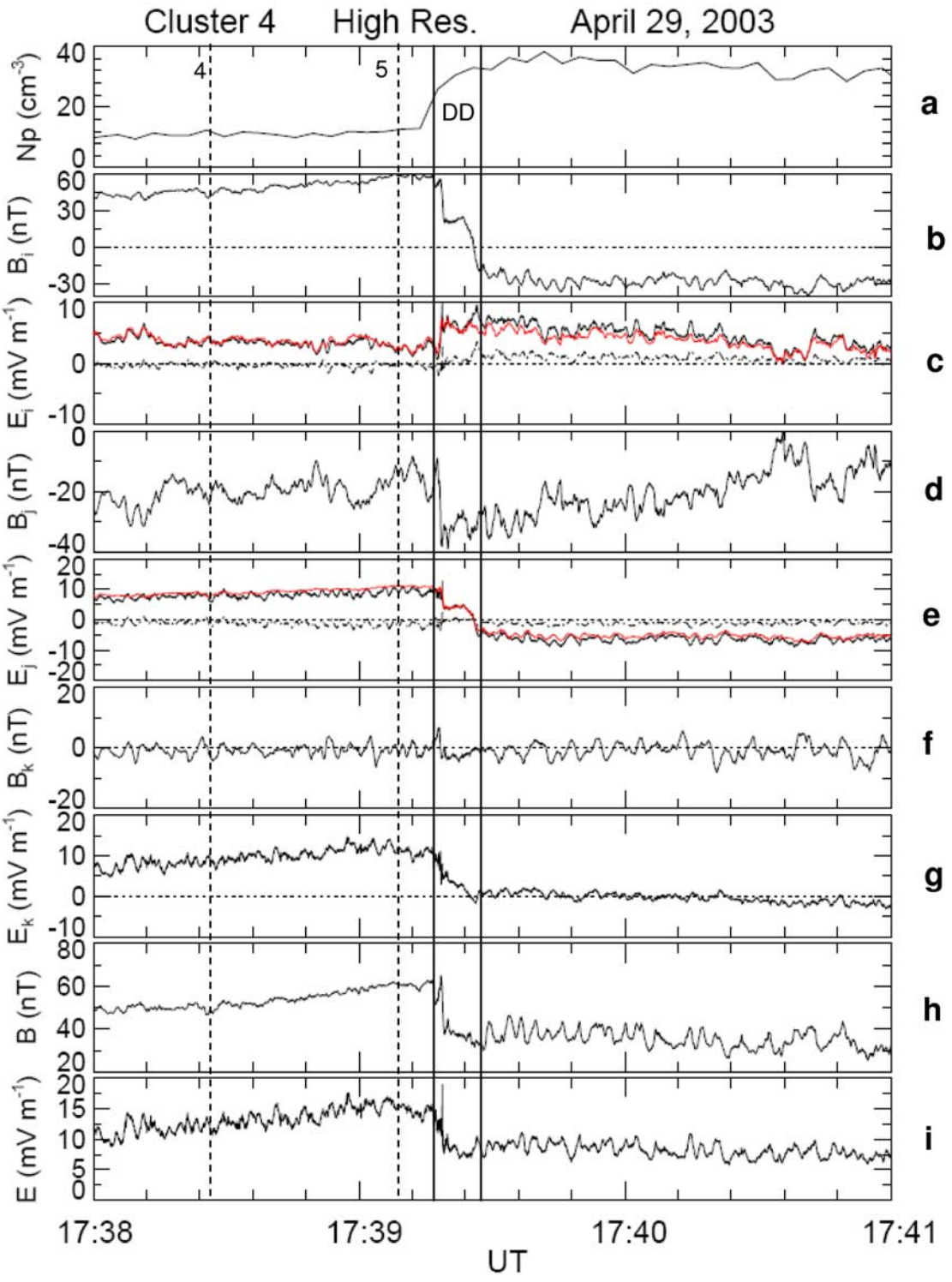

Figure 12. (a) The density. (b–g) The components of the magnetic and electric fields in minimum variance coordinates (i, j, k). (h–i) The magnitudes of the magnetic and electric fields. In Figures 12c and 12e, the red traces are the components of $-\mathbf{V_{TD}} \times \mathbf{B}$, where $\mathbf{V_{TD}}$ is the velocity of the TD calculated by triangulation. The dashed traces near zero are the differences between the measured electric fields and $-\mathbf{V_{TD}} \times \mathbf{B}$. The first vertical line marks the start of the TD (used for triangulation calculations), while the second marks the end. Lines 4 and 5 mark the slow-mode feature.

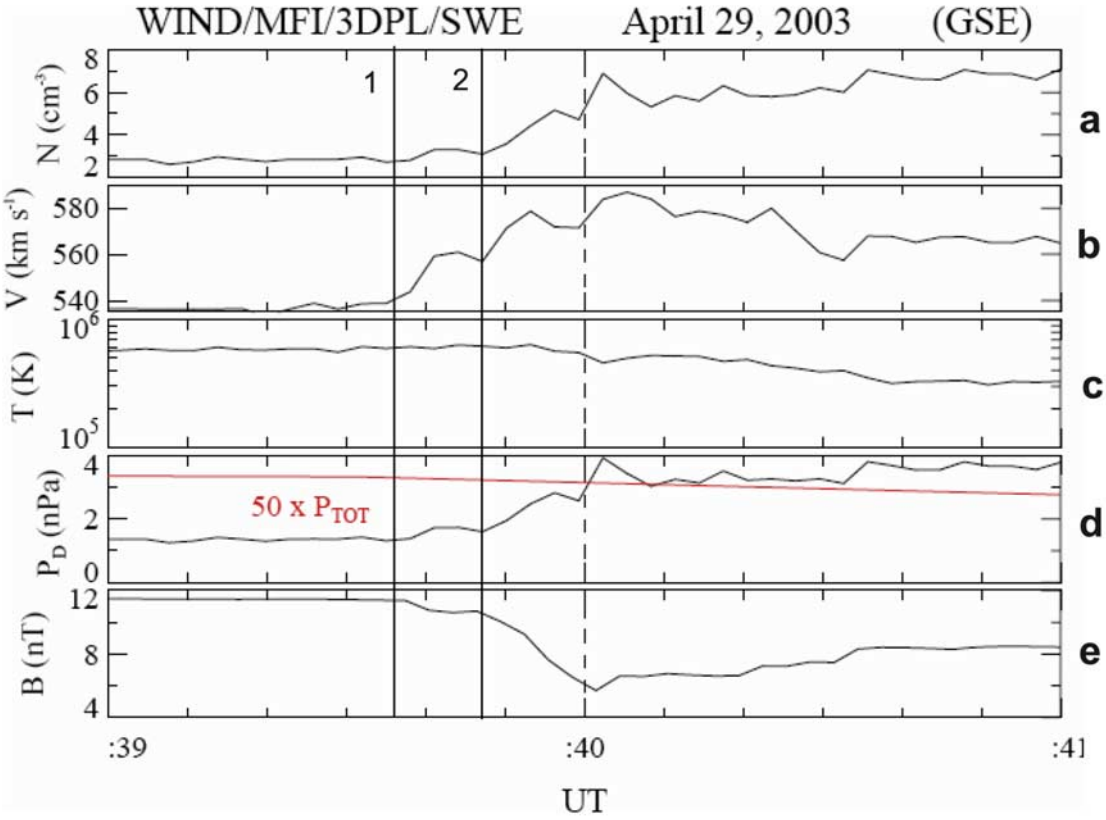

Figure 13. The density, velocity, temperature, dynamic pressure, and magnitude of **B** measured by Wind in the 2 min centered on the TD.

times with the accuracy needed for triangulation. If it is a small-amplitude fast shock, it must propagate at a fast-mode speed, similar to the main fast shock starting at line 2. We have positioned line 1 in each trace of Figure 5 by putting it at the same Δt before line 2. The ratio of the measured FS velocity (456 km/s) to the TD velocity (188 km/s) is 2.42. If the variation starting at line 1 is caused by a weak fast shock from the small density and dynamic pressure change at Wind, then stretching the timescale of the Wind data by the factor 2.42 should make the correlation clear. The density and velocity traces from such a stretch are shown in Figure 3c and 3e, respectively. The starts of the two step increases at Wind on the stretched scale correspond well to lines 1 and 2 in Figure 3, establishing that both features are traveling at the magnetosonic speed. It appears reasonable to equate variations starting at line 1 to a weak fast shock, following a similar path as the main fast shock starting at line 2. The upward trend in the density was initiated by the two fast shocks.

[41] At different times just before encountering the TD all four spacecraft observed increases in $|\mathbf{B}|$ for similar durations (between dashed lines 4 and 5 in Figure 5). The density remained nearly constant (see Figure 3b for Cluster 1 variation) or slightly increasing (see Figure 7a for the first part of the Cluster 4 variation) during the passage of this structure. Considering the general increase in background density associated with the fast shock, the constant level can be regarded as a decrease from the trend. From this perspective, the density perturbation anticorrelates with the increase in $|\mathbf{B}|$. The triangulated velocity was 152.4 km/s in a GSE direction of (−0.9303, −0.1847, −0.3168), and significantly slower than the plasma bulk speed (250 km/s), the magnetosonic speed (>450 km/s), and the TD's velocity (188 km/s). The structure was propagating in the wrong direction for a fast wave reflected from the magnetopause. After subtracting the bulk flow measured by Cluster 4 of (−175, −105, 100) km/s (Figure 5) to shift to the plasma rest frame, the resulting velocity is 170 km/s in a GSE direction of (0.1949, 0.4515, −0.8708), at an angle of 60.5° relative to **B**. Using the slow-mode branch of equation (2) with V_A = 334 km/s, V_S = 323 km/s, and the 60.5°angle to **B**, we calculate that a slow-mode velocity is 137 km/s. This is comparable to the triangulated velocity, but significantly smaller than that in the plasma rest frame. The largest component is in the −Z direction. Figure 10d shows that the Z component of the velocity in the XY plane at Z = 6.5 and 207:30 simulation time, appropriate for the structure passing Cluster. At the location of Cluster (+) there is a dip in the upward velocity consistent with the negative perturbation of this slow-mode wave.

[42] *Neubauer* [1976] noted that fast shock-TD interactions can lead to the excitation of a variety of modes that propagate downstream and upstream from the interaction. One of these is a slow-mode wave. The start and end times of this structure differ with respect to the TD at the four spacecraft. Since the structure's triangulated velocity is slower than that of the TD, it cannot have been generated at the original interaction location of the TD with the bow

shock and still appear downstream of (i.e., earlier than) the TD. However, since the fast shock in our case is the bow shock standing in front of the Earth, the interaction is only locally planar and more complex.

[43] From the simulation we observe that when the fast mode wave is launched, a second structure containing a current in the Y direction and positive $\mathbf{J} \bullet \mathbf{E}$ appears close to the bow shock and TD. The fast shock and the structure separate in time, with the other structure staying just downstream of the TD. At the time the other structure in the simulation passed Cluster there is a $+J_Y$ (Figure 10h). As the fast shock propagates, its front remained planar, with its velocity being smaller than, but comparable to that of the solar wind velocity. In the magnetosheath the speeds of the TD and the slower structure are ~50% of solar wind values. Consequently interplanetary magnetic field lines bend and compress in magnetosheath near the bow shock. The interface between the TD and the bow shock moves down the flanks at the solar wind speed. This stretches field lines adding magnetic tension to the magnetic pressure in the $\mathbf{J} \times \mathbf{B}$ force.

[44] We note that the measured slow structure involves a compression of the magnetic field. In the plasma rest frame and the structure's velocity of is in the $+X$, $+Y$, and $-Z$ directions, placing its source above, toward dawn, and slightly behind the location of Cluster. This is in the direction of the bow shock's location as it curves back toward the flank.

6. Conclusions

[45] With the four Cluster spacecraft we have observed a fast shock generated from the interaction of a tangential discontinuity and accompanying pressure increase with Earth's bow shock on 29 April 2003. The discontinuity propagated earthward through the magnetosheath, upstream of the fast shock, and remained a TD at least until after it passed the Cluster location. We have used MHD simulations to help interpret the observations. In agreement with theory and the modeling work of *Völk and Auer* [1974] and *Wu et al.* [1993], the fast shock has the following properties:

[46] 1. Changes in density and $|\mathbf{B}|$ are correlated.

[47] 2. It propagated ahead of the TD in the magnetosheath at a speed comparable to the magnetosonic speed in the rest frame of the unshocked plasma with a direction nearly perpendicular to $\mathbf{B}$.

[48] 3. It carried a 20% increase in $|\mathbf{B}|$ and density and a 33% velocity increase.

[49] 4. The fast shock was planar, while the trailing TD surface became curved in the magnetosheath as its velocity is decreased from solar wind values.

[50] In addition, we make the following conclusions:

[51] 1. Simulations show that the fast shock was initiated by the density increase and not the TD's magnetic field change. The fast shock initiated the inward motion of the magnetopause toward a new equilibrium position consistent with increased upstream pressure.

[52] 2. A weak fast shock was observed about 30 s earlier which was apparently initiated by the weaker step of the two-step density increase observed at Wind. This highlights the fact that a fast shock can be expected from any step increase in density interacting with the bow shock, no matter how strong.

[53] 3. When the fast shock interacted with the magnetopause a reflected fast rarefaction wave, traveling at the magnetosonic speed in the rest frame of the plasma, was generated and observed by Cluster.

[54] 4. A current in the Y direction was observed by Cluster and seen in the simulation. Coupled with a positive E_Y, the positive $\mathbf{J} \bullet \mathbf{E}$ indicates that energy became available to heat particles. Indeed, energy increases were observed in ion spectra and temperature. The simulation predicted a positive $\mathbf{J} \bullet \mathbf{E}$ and temperature increase.

[55] 5. The DD was a TD when it passed the Wind spacecraft in the solar wind and remained one at least until after it had passed Cluster in the magnetosheath.

[56] 6. The TD's velocity in the magnetosheath was less than the plasma bulk velocity and was primarily in the $-X_{\mathrm{GSE}}$ direction, with values between the down- and upstream plasma velocity's X_{GSE} components. Velocity differences on both sides of the discontinuous surface pointed inward, consistent with the TD being compressed as it propagated toward the magnetopause. Velocity components tangential to the TD accounted for the larger bulk velocity magnitude.

[57] 7. A large-scale change in the structure (fluctuation level) of the magnetosheath was ushered in by the passage of the TD, which set up compressive oscillations in the magnetic field which satisfied the mirror mode instability criterion.

[58] A structure developed just downstream of the TD in the magnetosheath that moved slower than the plasma. Its velocity in the rest frame of the plasma was mostly in the $-Z$ direction. The simulation indicated a reduced $+V_Z$ in this region. The structure had slow-mode characteristics in that density and $|\mathbf{B}|$ perturbations anticorrelate. The structure's velocity was comparable to that of slow-mode disturbance propagating at an oblique angle to $\mathbf{B}$. The source of this structure appears to have been on the northward and dawnward sides of the Cluster constellation, probably near the bow shock.

[59] When a solar wind pressure increase occurs, the magnetopause position must move inward to maintain pressure balance. The removal, or erosion, of the magnetic flux between the old and new positions is accomplished by merging [e.g., *Siscoe et al.*, 2002; *Maynard et al.*, 2006; *Ober et al.*, 2007]. The timing of the initiation of these changes is determined by the arrival of the fast shock generated when the solar wind pressure increase crossed the bow shock.

[60] **Acknowledgments.** We are grateful to E. A. Lucek and the Cluster Magnetometer Team for use of the magnetic field data and to M. Andre for use of the Cluster electric field data. We thank R. P. Lepping, R. P. Lin, and K. W. Ogilvie for the use of the Wind magnetic field and plasma data. The ISM was developed under sponsorship of the Defense Threat Reduction Agency, 45045 Aviation Drive, Dulles, VA 20166–7517. ISM computations were performed on computers at AFRL. The work at the University of New Hampshire was supported by NASA through Cluster mission funding to the University of California, Berkeley (subcontracted). C.J.F. is also partially supported by NASA/SEC-GI grant NNG05GG25G and NASA Wind grant NNX08AD11G. W.J.B. and D.M.O. received funding support from the Air Force Office of Scientific Research.

[61] Zuyin Pu thanks the reviewers for their assistance in evaluating this manuscript.

References

Balogh, A., et al. (2001), The Cluster magnetic field investigation: Overview of in-flight performance and initial results, *Ann. Geophys.*, *19*, 1207–1217.

Décréau, P. M. E., et al. (2001), Early results from the Whisper instrument on Cluster: An overview, *Ann. Geophys.*, *19*, 1241–1258.

Dunlop, M. W., A. Balogh, K.-H. Glassmeier, and P. Robert (2002), Four-point Cluster application of magnetic field analysis tools: The curlometer, *J. Geophys. Res.*, *107*(A11), 1384, doi:10.1029/2001JA005088.

Fairfield, D. H., and N. F. Ness (1970), Magnetic field fluctuations in the Earth's magnetosheath, *J. Geophys. Res.*, *75*, 6050–6060, doi:10.1029/JA075i031p06050.

Friedricks, K. O. (1957), Wave motion in magnetohydrodynamics, *Rep. LAMS-2105*, Los Alamos Natl. Lab., Los Alamos, N. M.

Grib, S., B. Brunelli, M. Dryer, and W.-W. Shen (1979), Interaction of interplanetary shock waves with the bow shock-magnetopause system, *J. Geophys. Res.*, *84*(A10), 5907–5921.

Gustafsson, G., et al. (1997), The electric field and wave experiment for the Cluster mission, *Space Sci. Rev.*, *79*, 137–156.

Hain, K. (1987), The partial donor cell method, *J. Comput. Phys.*, *73*, 131–147, doi:10.1016/0021-9991(87)90110-0.

Hasegawa, A. (1975), *Plasma Instabilities and Non-linear Effects*, pp. 94–98, Springer, New York.

Kantrovitch, A., and H. E. Petschek (1966), *Plasma Theory and Applications*, edited by W. B. Kunkel, 158 pp., McGraw-Hill, New York.

Kivelson, M. G., and C. T. Russell (1995), *Introduction to Space Physics*, pp. 331–342, Cambridge Univ. Press, New York.

Knetter, T., F. M. Neubauer, T. Horbury, and A. Balogh (2004), Four-point discontinuity observations using Cluster magnetic field data: A statistical survey, *J. Geophys. Res.*, *109*, A06102, doi:10.1029/2003JA010099.

Lepping, R. P., and K. W. Behannon (1980), Magnetic field directional discontinuities: 1. Minimum variance errors, *J. Geophys. Res.*, *85*(A9), 4695, doi:10.1029/JA085iA09p04695.

Lepping, R. P., et al. (1995), The Wind magnetic field investigation, *Space Sci. Rev.*, *71*, 207–229, doi:10.1007/BF00751330.

Lin, R. P., et al. (1995), A three-dimensional plasma and energetic particle investigation for the Wind spacecraft, *Space Sci. Rev.*, *71*, 125, doi:10.1007/BF00751328.

Maynard, N. C., G. L. Siscoe, B. U. Ö. Sonnerup, D. R. Weimer, K. D. Siebert, G. M. Erickson, W. W. White, J. A. Schoendorf, D. M. Ober, and G. R. Wilson (2002), Predictions of magnetosheath merging between IMF field lines of opposite polarity, *J. Geophys. Res.*, *107*(A12), 1456, doi:10.1029/2002JA009289.

Maynard, N. C., et al. (2006), Characteristics of merging at the magnetopause inferred from dayside 557.7-nm all-sky images: IMF drivers of poleward moving auroral forms, *Ann. Geophys.*, *24*, 3071–3098.

Maynard, N. C., W. J. Burke, D. M. Ober, C. J. Farrugia, H. Kucharek, M. Lester, F. S. Mozer, C. T. Russell, and K. D. Siebert (2007), Interaction of the bow shock with a tangential discontinuity and solar-wind density decrease: Observations of predicted fast waves and magnetosheath merging, *J. Geophys. Res.*, *112*, A12219, doi:10.1029/2007JA012293.

Neubauer, F. M. (1975), Nonlinear oblique interaction of interplanetary tangential discontinuities with magnetogasdynamic shocks, *J. Geophys. Res.*, *80*, 1213–1222, doi:10.1029/JA080i010p01213.

Neubauer, F. M. (1976), Nonlinear interaction of discontinuities in the solar wind and the origin of slow shocks, *J. Geophys. Res.*, *81*, 2248–2256, doi:10.1029/JA081i013p02248.

Neugebauer, M. (2006), Comments on the abundances of rotational and tangential discontinuities in the solar wind, *J. Geophys. Res.*, *111*, A04103, doi:10.1029/2005JA011497.

Neugebauer, M., D. R. Clay, B. E. Goldstein, B. T. Tsurutani, and R. D. Zwickl (1984), A reexamination of rotational and tangential discontinuities in the solar wind, *J. Geophys. Res.*, *89*, 5395–6408, doi:10.1029/JA089iA07p05395.

Ober, D. M., G. R. Wilson, W. J. Burke, N. C. Maynard, and K. D. Siebert (2007), Magnetohydrodynamic simulations of transient transpolar potential responses to solar wind density changes, *J. Geophys. Res.*, *112*, A10212, doi:10.1029/2006JA012169.

Ogilvie, K. W., et al. (1995), SWE, a comprehensive plasma instrument for the Wind spacecraft, *Space Sci. Rev.*, *71*, 55–77, doi:10.1007/BF00751326.

Phan, T. D., G. Paschmann, C. Twitty, F. S. Mozer, J. T. Gosling, J. P. Eastwood, M. Øieroset, H. Rème, and E. A. Lucek (2007), Evidence for magnetic reconnection initiated in the magnetosheath, *Geophys. Res. Lett.*, *34*, L14104, doi:10.1029/2007GL030343.

Rème, H., et al. (2001), First multispacecraft ion measurements in and near the Earth's magnetosphere with the identical Cluster Ion Spectrometry (CIS) experiment, *Ann. Geophys.*, *19*, 1303–1354.

Russell, C., M. Mellott, E. Smith, and J. King (1983), Multiple spacecraft observations of interplanetary shocks: Four spacecraft determination of shock normals, *J. Geophys. Res.*, *88*(A6), 4739–4748.

Samsonov, A. A., D. G. Sibeck, and J. Imber (2007), MHD simulation for the interaction of an interplanetary shock with the Earth's magnetosphere, *J. Geophys. Res.*, *112*, A12220, doi:10.1029/2007JA012627.

Siscoe, G. L., N. U. Crooker, and K. D. Siebert (2002), Transpolar potential saturation: Roles of region 1 current system and solar wind ram pressure, *J. Geophys. Res.*, *107*(A10), 1321, doi:10.1029/2001JA009176.

Sonnerup, B. U. Ö., and L. J. Cahill (1967), Magnetopause structure and attitude from Explorer 12 observations, *J. Geophys. Res.*, *72*, 171–183, doi:10.1029/JZ072i001p00171.

Sonnerup, B. U. Ö., I. Papamastorakis, G. Paschmann, and H. Lühr (1987), Magnetopause properties from AMPTE/IRM observations of the convection electric field: Method development, *J. Geophys. Res.*, *92*, 12,137–12,159, doi:10.1029/JA092iA11p12137.

Southwood, D. J., and M. G. Kivelson (1992), On the form of the flow in the magnetosheath, *J. Geophys. Res.*, *97*, 2873–2879, doi:10.1029/91JA02446.

Southwood, D. J., and M. G. Kivelson (1995), Magnetosheath flow near the sub-solar magnetopause: Zwan-Wolf and Southward-Kivelson theories reconciled, *Geophys. Res. Lett.*, *22*, 3275–3278, doi:10.1029/95GL03131.

Spreiter, J. R., and A. Y. Alksne (1969), Plasma flow around the magnetosphere, *Rev. Geophys.*, *7*, 11–50, doi:10.1029/RG007i001p00011.

Tsurutani, B. T., E. J. Smith, R. R. Anderson, K. W. Ogilvie, J. D. Scudder, D. N. Baker, and S. J. Bame (1982), Lion roars and nonoscillatory drift mirror waves in the magnetosheath, *J. Geophys. Res.*, *87*, 6060–6072, doi:10.1029/JA087iA08p06060.

Völk, H. J., and R.-D. Auer (1974), Motions of the bow shock induced by interplanetary disturbances, *J. Geophys. Res.*, *79*, 40–48, doi:10.1029/JA079i001p00040.

White, W. W., J. A. Schoendorf, K. D. Siebert, N. C. Maynard, D. R. Weimer, G. L. Wilson, B. U. Ö. Sonnerup, G. L. Siscoe, and G. M. Erickson (2001), MHD simulation of magnetospheric transport at the mesoscale, in *Space Weather, Geophys. Monogr. Ser.*, vol. 125, edited by P. Song, H. J. Singer, and G. L. Siscoe, pp. 229–240, AGU, Washington, D. C.

Wu, B. H., M. E. Mandt, L. C. Lee, and K. K. Chao (1993), Magnetospheric response to solar wind dynamic pressure variations: Interaction of interplanetary tangential discontinuities with the bow shock, *J. Geophys. Res.*, *98*, 21,297–21,311, doi:10.1029/93JA01013.

Zwan, B. J., and R. A. Wolf (1976), Depletion of solar wind plasma near a planetary boundary, *J. Geophys. Res.*, *81*, 1636–1648, doi:10.1029/JA081i010p01636.

W. J. Burke and D. M. Ober, Air Force Research Laboratory, AFRL/RVBXP, 29 Randolph Road, Hanscom Air Force Base, MA 01713, USA.

P. Décréau, Laboratoire de Physique et Chimie de l'Environnement, F-45071 Orleans, France.

M. Dunlop, Rutherford Appleton Laboratory, Didcot OX11 0QX, UK.

C. J. Farrugia and N. C. Maynard, Space Science Center, University of New Hampshire, Durham, NH 03842, USA.

F. S. Mozer, Space Science Laboratory, University of California, Berkeley, CA 94720, USA.

H. Rème, CESR, CNRS, BP 4346, F-31028 Toulouse, France.

K. D. Siebert, SPARTA Inc., 39 Simon Street, Suite 15, Nashua, NH 03062, USA.